Computations of pressure loads on an oscillating water column with experimental comparison for random waves

Marc Batlle Martin, Grégory Pinon, Gabriel Barajas, Javier Lara, Julien Reveillon

Coastal Engineering

Computations of pressure loads on an oscillating water column with experimental comparison for random waves ☆

Marc Batlle Martin [a,d,e,*], Grégory Pinon [a], Gabriel Barajas [b], Javier L. Lara [b], Julien Reveillon [c]

[a] Laboratoire Ondes et Milieux Complexes, Normandie Univ, UNIHAVRE, CNRS, LOMC-UMR 6295, Le Havre, France
[b] IHCantabria, Instituto de Hidráulica Ambiental de La Universidad de Cantabria C/Isabel Torres No 15, Parque Científico y Tecnológico de Cantabria, 39011, Santander, Spain
[c] Complexe de recherche interprofessionnel et arothermochimie, CORIA-UMR 6614, CNRS - Normandie Univ. UNIROUEN, Rouen, France
[d] France Energies Marines, Plouzané, Bretagne, France
[e] Laboratoire d'Hydraulique Saint-Venant, EDF R&D, Chatou, France

ARTICLE INFO

Keywords:
Air compressibility
Irregular waves
OpenFOAM
Oscillating water column
Wave loads
Wave energy converters

ABSTRACT

This paper presents numerical investigations with experimental comparisons of random wave induced loads on the external walls of a large scale Oscillating Water Column (OWC) device. The objective is to investigate the capability of a numerical model that uses the Reynolds Averaged Navier–Stokes (RANS) equations to accurately reproduce extreme wave loads on an OWC. Both incompressible and compressible approximations for the RANS equations are studied in this work with the aim of investigating the limitations of both approaches. After a first characterisation of the random wave propagation processes at the numerical flume, wave loads are analysed. An OWC power take-off (PTO) and in-chamber air compressibility effects are studied using regular waves. Next, an OWC facing irregular waves is studied and compared with experimental data, putting special emphasis on the extreme loads together with the stochastic nature of random waves. The simulation of extreme wave loads on an OWC is validated and the necessity of a compressible model for correct reproduction of an OWC in-chamber flow for certain operating conditions of the PTO is pointed out from the simulations.

1. Introduction

An oscillating water column (OWC) is a wave energy converter (WEC) which makes use of the potential energy of waves for producing clean energy by controlling a piston type mechanism within a chamber and causing turbine rotation. A power take-off (PTO) can be integrated within a breakwater caisson, see Jarlan (1961), Takahashi et al. (1985), Takahashi (1988), He and Huang (2016), Vicinanza et al. (2019), allowing some cost sharing between the harbour protection and energy generation functions. Such an engineering structure has already been tested in Sakata harbour (Japan) (Suzuki et al., 2004), Pico Island in Açores (Portugal) (Neumann and Crom, 2011; Falcã A.F. Sarmento et al., 2020) or in Mutriku (Spain) (Torre-Enciso et al., 2009), among others.

Experience from previous OWC prototypes deployments has shown that wave loads are often underestimated on these kind of devices, possibly leading to severe structural damages. For instance: very important damages occurred on the PICO prototype in the Açores and also severe damages append to four of the 16 OWC chambers, including the loss of the entire front wall of one chamber in Mutriku (see Medina-Lopez et al. (2015) for more detail on this precise case). These arise the necessity of revisiting the existing wave loads predicting formulations for a proper assessment of the structure survivability.

Extreme wave impacts are commonly encountered when breaking waves impact coastal structures, producing very large forces over a very short period of times. This phenomenon has been largely investigated, Stevenson (1840) or de Rouville et al. (1938). The wide range of pressure records for apparently very similar wave impacts and the importance of air during wave breaking was already early reported by Bagnold (1939). In 1977, a general formulation for wave pressure on a caisson breakwater was proposed by Goda (2010) and extended for breaking waves impacts by Shigeo Takahashi and ichiro Shimosako (1993).

Cooker and Peregrine (1990) by means of a potential boundary integral numerical model, signalled that the most intense impacts were generated by breaking waves with small amounts of air. This was corroborated experimentally by Hattori et al. (1994) attributing the

(a) (b)

Fig. 1. Pictures from the experimental setup during the installation and the OWC undergoing wave impacts.
Source: Credit: Allsop et al. (2014).

reduction of pressure maximum values and the increase on the peak pressure rise time to large amounts of air entrapped between the water and the solid structure. A classification of the different wave loads based on the recorded pressure signal was proposed by Oumeraci et al. (2001), differentiating between pulsating and impact loads. This was further investigated experimentally by Bullock et al. (2007) who reported pressure magnitudes up to 150 times the wave height pressure head.

Nevertheless, extreme wave loads on OWC have been less investigated. In the work entitled *Large scale tests on a generalised oscillating water column wave energy converter*, carried out in the GWK wave flume by Allsop et al. (2014), a wide range of sea-state conditions were tested and the exerted loads on the OWC front and inner walls were recorded. Results from these experiments were later further investigated and analysed by several authors, see Viviano et al. (2016, 2019), Pawitan et al. (2019, 2020), and even some initial attempts to model these experiments numerically were carried out by Dimakopoulos et al. (2015) with some limitations by assuming the fluids as incompressible. These works achieved to describe the observed wave loads on the structure carapace and proposed a semi-analytical model to predict the non-breaking waves loads on the carapace. The exact same experimental set-up is also employed in the present work in order to enable numerical-experimental comparison and validation.

The necessity of reinforcing and constructing innovative coastal defensive structures, together with the global emissions objectives to increase the renewable energy sources, has motivated the present study to assess an OWC device facing extreme sea states included in a vertical breakwater. More precisely, the aim of the present paper is to investigate whether a numerical assessment is capable of accurately reproducing such wave impact on OWC. Moreover, it is well-known that the in-chamber flow, possibly coupled with the PTO mechanism modify the overall flow. Is-it possible, with such a numerical approach, to assess possibly extreme wave loading taking into account an irregular wave train, in-chamber flow computation together with the account of the PTO influence?

The present paper will try to answer this question using the OpenFOAM (Weller et al., 1998) software and following a methodology of successive computation/validation of increasing complexity configuration. Therefore, the paper is organised as follows: Section 2 briefly describes the aforementioned experimental configuration (Allsop et al., 2014) and a filtering of the experimental pressure records because high acquisition frequencies can lead to noisy signals. Then, the numerical method core equations as well as the relaxation zone method for wave generation are introduced in Section 3. Moreover, in this section, 2D simulations of regular and random waves are presented and used for a sensitivity analysis. Then, Section 4 is dedicated to the validation of numerical models solving an OWC with a PTO as a whole system subjected to regular waves. And finally, Section 5, presents an extensive study and validation of extreme loads on an OWC front wall equipped with a PTO produced by various irregular sea-states that were experimentally tested by Allsop et al. (2014).

2. Experimental configuration

2.1. Experimental set-up

The forthcoming numerical results will be compared with the experimental data-sets obtained from Allsop et al. (2014). This experimental study was led by Dr. Tom Bruce in the Grosse Wellenkanal (GWK, see Fig. 1) under the Hydralab IV project. Several authors already analysed the obtained experimental results. On the one hand, Viviano et al. (2016, 2019) characterised reflection coefficients, exerted pressures on the exterior and interior of the OWC curtain wall, and compressibility effects inside the OWC chamber. On the other hand, and more recently, Pawitan et al. (2019, 2020) further explored the wave loads and pressures on the structure front wall. Dimakopoulos et al. (2015) numerically reproduced the chamber behaviour under regular waves. However, an incompressible solver was employed at that time, which presented some limitations under certain circumstances. It will be detailed in Section 4. Nevertheless, Dimakopoulos et al.'s results will be used in the present work for comparison and further validation.

Allsop et al. (2014)'s experiments were designed at a nominal Froude scale of approximately 1:9 relative to the prototype. The flume was 307 m long, 7.0 m deep and 5.0 m wide and the OWC structure (Fig. 2) was built 97.5 m away from the piston paddle wave-maker. The structure was composed of 3 chambers (Fig. 1(a)), with a 1 in 6 slope rising from the flume floor to the structure foot (see bottom left of Fig. 2).

Multiple wave gauges (WG01-WG04) were located halfway between the wave-maker and the structure and three other gauges in front of the structure (WG05-WG08). The central caisson was equipped with five free-surface elevation gauges (WG09-WG13) inside the chamber, which can clearly be identified from the schematic representation of Fig. 2. The acquisition frequency for all wave gauges was set to 100 Hz. The central caisson was also equipped with multiple pressure transducers (General Electric Druck PDCR 1830) measuring air and water-induced pressures on the front face, internal back wall and roof of the caisson. These pressure transducers are also clearly identifiable from Fig. 2. The pressure transducers sampling rate was set to 1 kHz for all test cases.

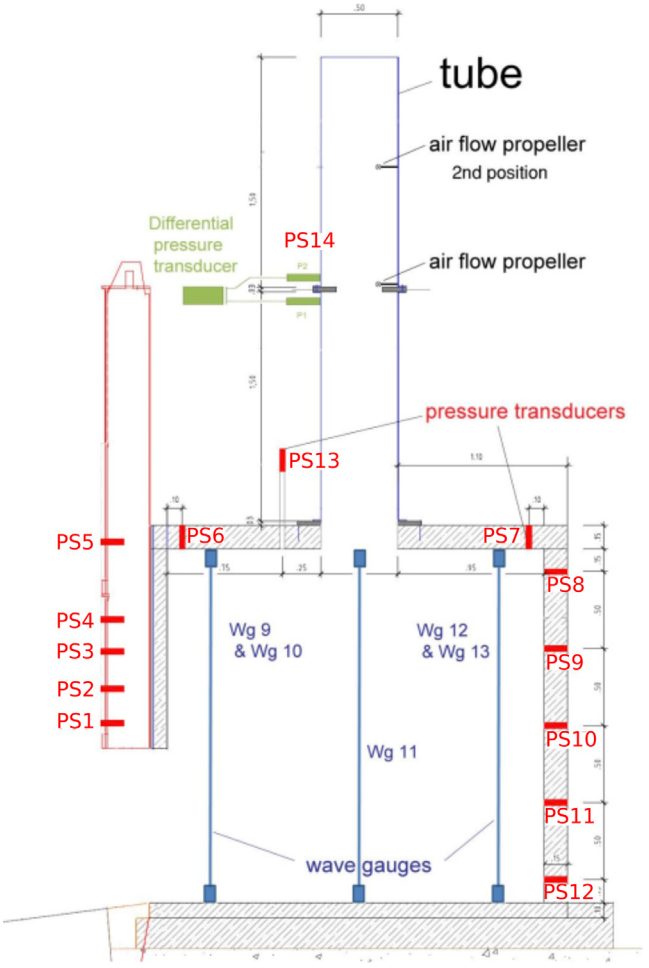

Fig. 2. Cross section of OWC model, showing (qualitatively) the locations of pressure transducers (red) and wave gauges (blue).
Source: Credit: Allsop et al. (2014).

Finally, a differential pressure transducer also measured the effects of an adjustable orifice. This adjustable orifice was installed to control air flows in and out of the caissons chambers, via the 0.5 m diameter tubes or chimneys (see Figs. 1 and 2), altogether mimicking Power Take-Off (PTO) devices. Various openings of the adjustable orifice were tested during the experiments. These experimental configuration will be referred as (d_0/D), where d_0 stands for the opened orifice diameter and D stands for the chimney diameter. A value of $d_0/D = 0$ means a completely closed orifice whereas $d_0/D = 1$ represents a fully opened situation. This ratio is expected to have a great influence on the chamber's hydraulic behaviour, e.g., using small ratios implies that the air inside the chamber will enhance compressibility effects. The experiments were run through a series of regular ($Reg\#$) and random or irregular ($Irr\#$) wave conditions. From Allsop et al. (2014)'s work, the relevant configurations for the present study are detailed in Table 1.

2.2. Experimental data analysis

During the experiments, all pressure transducers had a high acquisition frequency of 1 kHz. This was necessary to accurately describe possible impulsive loads related to breaking waves. However, this induced a non-negligible noisy characteristic of the recorded signal and occurrences of some nonphysical oscillations. This issue was already addressed in Viviano et al. (2016) for the impulsive pressure series. But the lack of information has motivated the present authors to develop a new filter for a better assessment and understanding of these experimental pressure signals. The authors would like to acknowledge the "HyIV-FZK-02" project (Allsop et al., 2014), for providing all the raw recorded files from the aforementioned experimental campaign.

Regarding the configurations without any impulsive event, the temporal scale of all the relevant phenomena is at least 0.1 s, which is two orders of magnitude larger than the acquisition time step of 1 ms. Under this assumption, three main aspects are addressed for filtering the original signal, as depicted in Fig. 3.

1. First, some scattered values can easily be identified as the one depicted at the bottom right of Fig. 3(b) ($t \approx 879$ s). These scattered values are removed from the series using a filter (Eq. (1)) based on a local variance:

$$\left(p(t_i) - p(t_{i\pm1})\right)^2 > 25 \cdot \left[\frac{1}{100}\sum_{n=i-50}^{i+50}\left(p(t_n) - \overline{p}(t_{i-50} < t < t_{i+50})\right)^2\right], \tag{1}$$

   where $\overline{p}$ refers to the mean value within the interval. Each pressure value $p(t_i)$ difference with the previous and the following value (t_{i-1}, t_{t+1}), where t_i is the current time-step, is compared against the average variance of the 50th previous and following values. If one of the local differences is higher than 25 times the local variance, the value is removed from the signal. The choice of 50 experimental time steps was motivated by the fact that it represents a duration of 0.05 s which is still lower than the aforementioned temporal characteristic of 0.1 s.
2. Secondly, a smoothing filter is used by means of a moving average of each value $p(t_i)$ over the (t_{i-50}, t_{t+50}) consecutive values (Fig. 3(c)). Again, this moving average is performed over a time scale of 0.05 s which is sufficiently small to prevent from an excessive smoothing.
3. Finally, a qualitative analysis is carried out for the two highest pressure sensors (PS 04–05) by observing if any wave reached those elevations. To do this, the instants related to the highest waves are identified by looking at the pressure series (p_{max}) from (PS 01–02–03). Then, the pressure series from (PS 04–05) are observed at those instants and if there is any relevant pressure rebound occurring (Fig. 3(d)), it is assumed that the wave did not reach that elevation. If any of the two highest waves observed is captured by the two highest pressure sensors (PS 04–05), it can be concluded that the pressure signal related to wave loads is zero at that location.

3. Numerical model

3.1. Numerical model

In this section, the numerical model assumptions and core mathematical equations are introduced. All the simulations in the present work are performed in two-dimensions (2D). A multiphase solver is chosen using a finite volume spatial discretisation and Volume Of Fluid (VoF) to track the free surface between phases, namely, air and water. Following the conclusions of Batlle Martin et al. (2021), the present work alternates between two approaches, incompressible and compressible, to correctly address different conditions when required. The considered formulation is properly indicated throughout the text.

The Navier–Stokes (NS) equations ensure the momentum and mass conservation at every cell. The linear momentum conservation equation takes the form:

$$\frac{\partial \rho \mathbf{u}}{\partial t} + \nabla \cdot (\rho \mathbf{u} \otimes \mathbf{u}) = \\ -\nabla p_d - \mathbf{x} \cdot \mathbf{g} \nabla \rho + \nabla \cdot \left[\mu \left(2\underline{\mathbf{S}} - \frac{2}{3}(\nabla \cdot \boldsymbol{u})\underline{\mathbf{I}}\right)\right], \tag{2}$$

Table 1
Summary of the wave conditions used as wavemaker's input in the present study.
Source: Selection from previous (Allsop et al., 2014)'s work.

Regular waves						
Ref	H [m]	T [s]	h [m]	H/λ [–]	h/λ [–]	d_0/D [–]
*Reg*6.05	0.4	4	3.5	0.020	0.17	0.6
*Reg*6.10	0.4	4	3.5	0.020	0.17	0.1
Irregular waves						
Ref	H_s [m]	T_p [s]	h [m]	H_s/λ_p [–]	h/λ_p [–]	d_0/D [–]
*Irr*01.10	0.26	3	3.5	0.020	0.27	0.6
*Irr*13.01	0.26	4.5	3.5	0.011	0.15	0.4
*Irr*11.07	1.0	6.0	3.5	0.030	0.11	0.4

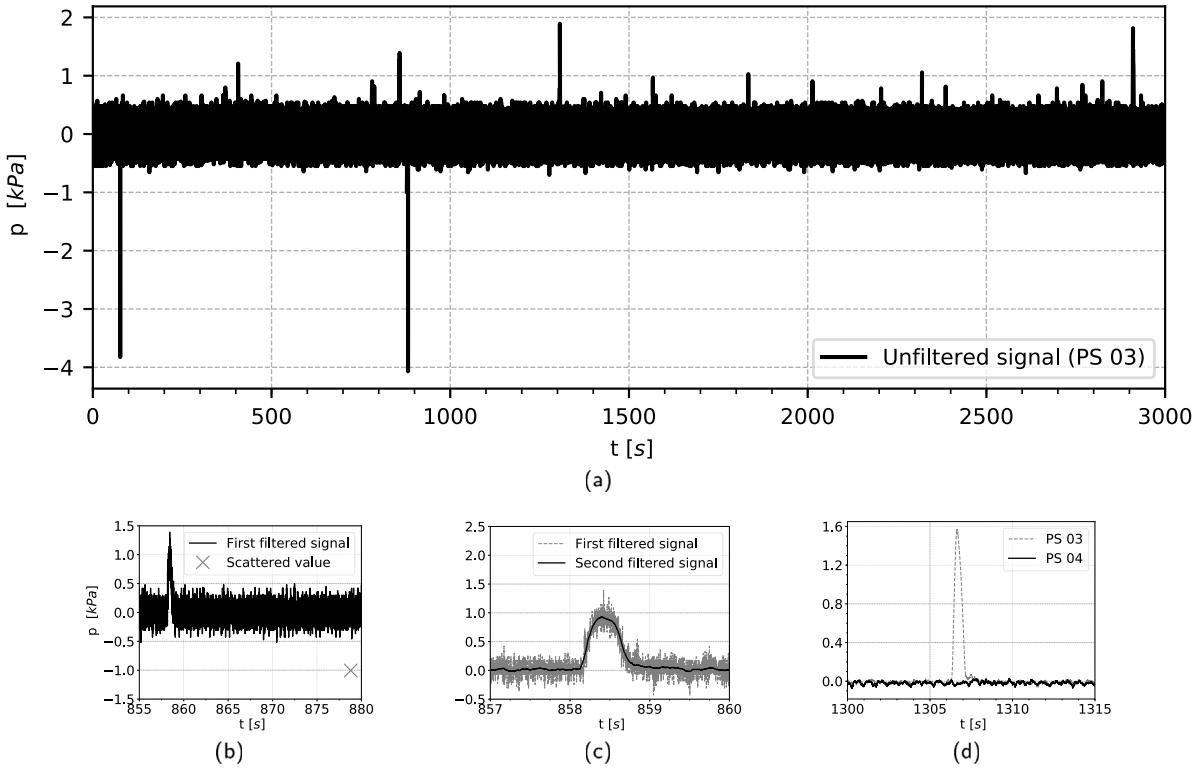

Fig. 3. Pressure signal recorded by transducer (PS 3), located on the front wall. Test conditions of Irr01.10 are: $H_S = 0.26$ m, $T_P = 3$ s and $d_0/D = 0.6$.

where ρ is the phase density, $\mathbf{u}$ is the cell centred velocity vector, $\otimes$ is the outer product, $p_d = p - \rho \mathbf{x} \cdot \mathbf{g}$ is a relative modified pressure introducing a density gradient near the interface, μ the dynamic viscosity, $\underline{\mathbf{S}}$ the strain rate tensor and $\underline{\mathbf{I}}$ the identity tensor. The last term in the right-hand side of Eq. (2), which accounts for compressibility effects, vanishes for incompressible flows. The flow configurations presented in this study are assumed to be driven inertial flows and thus, the surface tension effects are neglected for the sake of simplicity. Depending on the studied configuration, turbulence is either neglected or modelled by a $k-\omega$ SST turbulence model in cases where wave breaking occurs, as it is properly indicated throughout the text. For each tested configuration, a rationale will be given for the use or the absence of any turbulence model and these decisions are based on previous studies summarised in Windt et al. (2018, 2021). For the incompressible flows, a modified version of the $k-\omega$ SST turbulence model is used following the study of Larsen and Fuhrman (2018) but, when the compressible approach is chosen, a standard version of the $k-\omega$ SST is employed.

In order to model two phases, a new variable namely liquid volume fraction α, is introduced as:

$$\alpha = \frac{\rho - \rho_{air}}{\rho_{water} - \rho_{air}} , \tag{3}$$

taking values of 1 for water and 0 for air. Where ρ_{air} is the air density and ρ_{water} the water density. The liquid volume fraction transport equation, using a Multi-dimensional Limiter for Explicit Solution (MULES, see for instance (Deshpande et al., 2012)), for a compressible flow reads:

$$\frac{\partial \alpha}{\partial t} + \nabla \cdot (\alpha \mathbf{u}) = \alpha(1-\alpha)\left(\frac{\psi_{air}}{\rho_{air}} - \frac{\psi_{water}}{\rho_{water}}\right)\left(\frac{\partial p}{\partial t} + \boldsymbol{u} \cdot \nabla p\right) , \tag{4}$$

where the right-hand side of the equation takes into account the compressibility effects and would be zero for incompressible flows. The constant $\psi = \partial\rho/\partial p$ is the coefficient of compressibility (ψ_{air} for air and ψ_{water} for water) given by the equation of state (Eq. (5) or (6)) and the thermodynamics process.

Finally, when modelling compressible flows, the system is closed by means of equations of state (EOS). On the one hand, air is treated as an ideal gas undergoing an isentropic process and the equation of state reads:

$$\frac{p}{\rho^{\gamma}} = a_c = const. , \tag{5}$$

where $\gamma = 1.4$ denotes the ratio of (constant) specific heats and a_c is the isentropic constant. On the other hand, water undergoing an isentropic

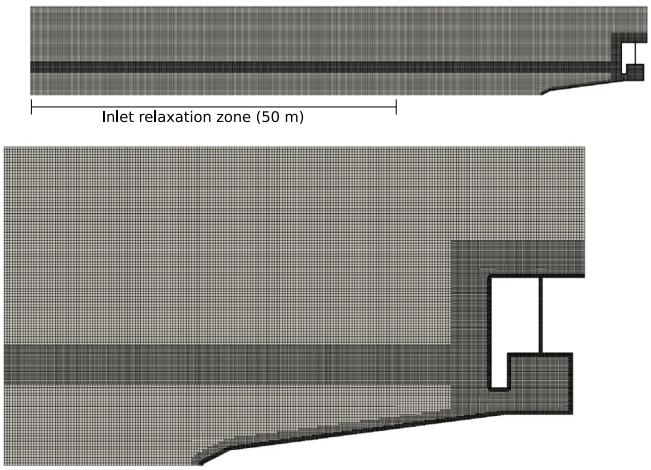

Fig. 4. Full mesh snapshot and a detail of the mesh in the vicinity of the OWC.

process is modelled using a weakly compressible or stiffened equation of state:

$$p + p^* = (\gamma - 1)e\rho \ , \tag{6}$$

where $\gamma = 7$ is the specific heat ratio and e is the internal energy per unit mass. Last Eq. (6) presents a modification of the standard EOS for perfect gas presented in Cole (1948) adding the empirical constant p^* which depends on the phase speed of sound. Under the isentropic process assumption, the energy equation is then neglected in the present work.

Among the best-known contributions of boundary conditions for wave generation and absorption, one can cite static or dynamic wave generators (Higuera et al., 2013) and relaxation zone techniques (Jacobsen et al., 2012). Here, the latest has been chosen motivated by an apparently better absorption of reflected waves in the present configuration of intermediate-deep water conditions. The relaxation zone method makes use of a domain region to ramp up to the target field values φ_{target} of velocities and liquid volume fraction field according to the selected wave theory. For this, a blending function is proposed as:

$$\varphi(\boldsymbol{x}, t) = \gamma_R(x)\varphi_{computed}(\boldsymbol{x}, t) + (1 - \gamma_R(x))\varphi_{target}(\boldsymbol{x}, t) \ , \tag{7}$$

where the weight field reads

$$\gamma_R = 1 - \frac{exp(\chi_R^{3.5}) - 1}{exp(1) - 1} \ . \tag{8}$$

Then, the target solution will be fully imposed at the boundaries $\gamma_R = 0$ and $\chi_R \in [0, 1]$ being a local coordinate within the relaxation zone. Towards the domain interior, γ_R changes smoothly to 0 to force the fully computed solution.

3.2. Numerical domain set-up

The employed numerical wave flume used to validate the experiments previously detailed in Section 2.1 is 84 m long and 12 mi high using a 2D configuration. The waves are generated using a relaxation zone of 50 m long (see top of Fig. 4) having the possibility to allocate approximately one wavelength in the present conditions. Boundary conditions are set to solid wall with a no-slip condition for the flume bottom, sloping beach and structure. While the top boundary is left as an open boundary imposing a total pressure condition, where air and water can freely flow out and only air can flow in. The computational domain is discretised into a structured grid (see Fig. 4). Δx is defined as the horizontal cell size and Δz the vertical one. The grid cell size is selected to maintain an aspect ratio $\Delta x/\Delta z = 1$ throughout the entire computational domain with a characteristic value of $\Delta x = 0.1$ m. To optimise computational times, a variable grid is defined (see bottom of Fig. 4), with a higher resolution around the free surface and close to the structure and beach boundaries. In these refinement areas, Δx is reduced (divided by 2) to obtain a value of $\Delta x = 0.05$ m. These values were selected after a sensitivity analysis presented in Appendix A and they allow to reduce the computational time costs while keeping a good accuracy. Finally, a second grid refinement is also performed very close to the sloping beach and on the structure walls with a value of $\Delta x = 0.025$ m.

An adaptive time-stepping is employed for the time discretisation using a maximum Courant number `maxCo`= 0.4 (`maxCo`= $mag(U) \cdot \Delta t/\Delta x$, where $mag(U)$ is the velocity magnitude, Δx the cell length and Δt is the time step) in the vicinity and away from the free surface. All the simulations that will be presented and compared with the experimental data are summarised in Table 2.

All over the paper, one regular and three irregular wave conditions will be tested. The major difference between the three random sea-states is the wave steepness, defined as $s = H_s/\lambda_p$. In the present study, random waves are generated using $N = 100$ wave components and a random phase seed. Increasing the number of wave components has shown to proportionally increase the computational time consumption without any clear improvement of the solution. The total simulated time length is defined as $1000\,T_p$ to capture the statistical properties of the considered irregular sea state. For the higher wave steepness configuration ($s = 0.03$), breaking waves were occurring even in the foreshore. As a consequence, the numerical time step was dropping regularly. Therefore and only for this wave configuration, the simulated time length duration was set to $1000/3\,T_p$ to avoid a skyrocketing computational cost. On the contrary, when using regular waves, the physical time duration is defined as $25\,T$.

The selected configurations (Table 2) are designed to cover the different relevant phenomena involved in a near-shore sea-state acting on an OWC. The principal objectives of the regular waves configurations are the investigation of the PTO modelling and the in-chamber compressibility effects. For this reason, incompressible and compressible models are compared. Simulating non-breaking regular waves and considering the boundary layer effects to remain out of the scope of the present work, a laminar approach is considered to be sufficient. On the other hand, the irregular waves configurations are specifically selected to investigate the response of the structure facing three different global spectral steepness. The necessity of modelling turbulence, due to wave breaking, in the last targeted configuration (Irr11.07) has motivated the use of a commonly employed turbulence model for marine hydrodynamics (i.e. $k-\omega$ SST, see Iturrioz et al. (2015), Elhanafi et al. (2017), or a modified version when available, see Larsen and Fuhrman (2018)) in all the irregular configurations. Moreover, the compressible and incompressible models are activated or deactivated when air-pockets (Irr11.07) or possible in-chamber compressibility effects (Irr13.01) are encountered.

4. OWC chamber assessment under regular waves

This section aims to characterise the behaviour of both fluids (water and air) inside the OWC chamber. Following the experimental work of Dimakopoulos et al. (2015), the exact same configuration is also chosen using regular wave conditions. The wave parameters are those presented in the previous Section 3.2 and validated in Appendix A. However, two configurations are now considered where the main difference lies in the orifice opening within the airflow tube (see Table 1). This adjustable orifice is modelled numerically by utilising a porous membrane obeying the Darcy–Forchheimer law, according to:

$$\frac{\nabla P}{\rho g} = a\mathbf{u} + b|u|\mathbf{u} \ , \tag{9}$$

where a, b are the Darcy and Forchheimer coefficients, respectively.

Table 2
Summary of simulations parameters. maxCo=0.4 and the use of MULES are considered for all computations.

Regular waves					
Ref	H/Δz [–]	λ/Δx [–]	Solver [–]	Turbulence [–]	Physical time [s]
*Reg*6.05					
	8	400	incompressible	laminar	100
	8	400	compressible	laminar	100
*Reg*6.10					
	8	400	incompressible	laminar	100
	8	400	compressible	laminar	100

Irregular waves						
Ref	$H_s/\Delta z$	$\lambda_p/\Delta x$	H_s/λ_p	Solver	Turbulence	Physical time
*Irr*01.10						
intermediate	5	262	0.02	incompressible	*mod* $k-\omega$ SST	3000
refined	7	349	0.02	incompressible	*mod* $k-\omega$ SST	3000
*Irr*13.01						
	5	466	0.01	incompressible	*mod* $k-\omega$ SST	4500
	5	466	0.01	compressible	$k-\omega$ SST	4500
*Irr*11.07	20	657	0.03	compressible	$k-\omega$ SST	2000

This is introduced in the momentum equation as a drag force based on empirical considerations acting only on the porous region. It is well known that impulse turbines, commonly used for converting pneumatic power to shaft power, have a non-linear behaviour (Anand et al., 2007). Thus, in the present work only the quadratic term is kept ($a = 0$) and, for an orifice plate, the resistance coefficient can be calculated using:

$$b \cdot \Delta L = \frac{\left[1 - C_C\left(\frac{d_0}{D}^2\right)\right]^2}{C_C^2\left(\frac{d_0}{D}^4\right)}, \tag{10}$$

where ΔL is the porous medium length and C_C is an empirical contraction coefficient as detailed in Miller (1978). Then, the parameter b takes values of $3{\times}10^5$ using $d_0/D = 0.1$ and 10^2 using $d_0/D = 0.6$.

Following the methodology proposed by Dimakopoulos et al. (2015) for analysing the results, the free surface evolution inside the chamber is assessed by averaging the temporal records of the three wave gauges (WG10, WG11, WG12) as depicted in Fig. 2. The averaging procedure was performed over 5 wave gauges during the experiments to account for any possible 3D effects, which was not possible here in this 2D numerical approach.

Four selected snapshots are presented in Fig. 5 during an oscillating process caused by regular incoming waves (test case Reg6.10 of Table 1). The presented results (Fig. 5) are those obtained using the compressible solver and orifice opening is defined as $d_0/D = 0.1$. In the first image ($t/T = 11.25$), the free-surface elevation is near the still water level while it is going down and an incoming wave approaches the trough. Air pressure inside the chamber has the minimum sub-atmospheric values and air is rapidly flowing inside the chamber. Next, for $t/T = 11.50$, air is still flowing into the chamber while the incoming wave approaches the structure. Free-surface elevation approximates its minimum and in-chamber pressure is close to atmospheric value. Free-surfaces inside and outside the chamber have similar elevation. At $t/T = 11.75$, air inside the chamber is fully compressed and flows out rapidly through the tube. The wave reaches the highest run-up on the front exterior wall and the free surface inside the chamber is again close to the still water level. In the last snapshot ($t/T = 12$), air is still flowing out from the chamber while the wave is reflected back from the structure. Free-surface elevation approximates its maximum and the pressure is close to the atmospheric values. A vortical structure is observable close to the bottom corner of the curtain wall.

The two tested configurations with regular waves are those Table 1, where two different orifice openings $d_0/D = 0.6$ and 0.1 are presented. As air compressibility inside the chamber may play a major role, especially when the orifice is nearly closed, the two compressible and incompressible numerical approaches are tested here. The present

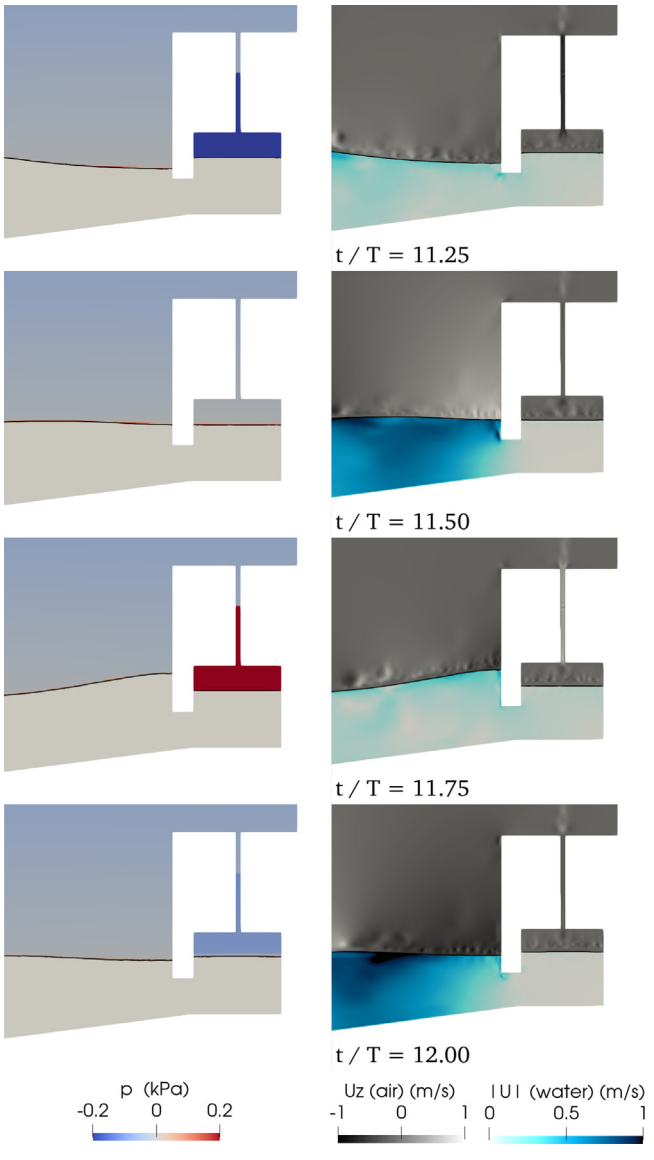

Fig. 5. Snapshots of four relevant instants of an OWC undergoing an air-chamber compression and expansion process related to Reg6.10 of Table 1. Each instant presents the gauge pressure for air (left panel), the velocity magnitude for water and vertical velocity for air (right panel), near and inside the chamber.

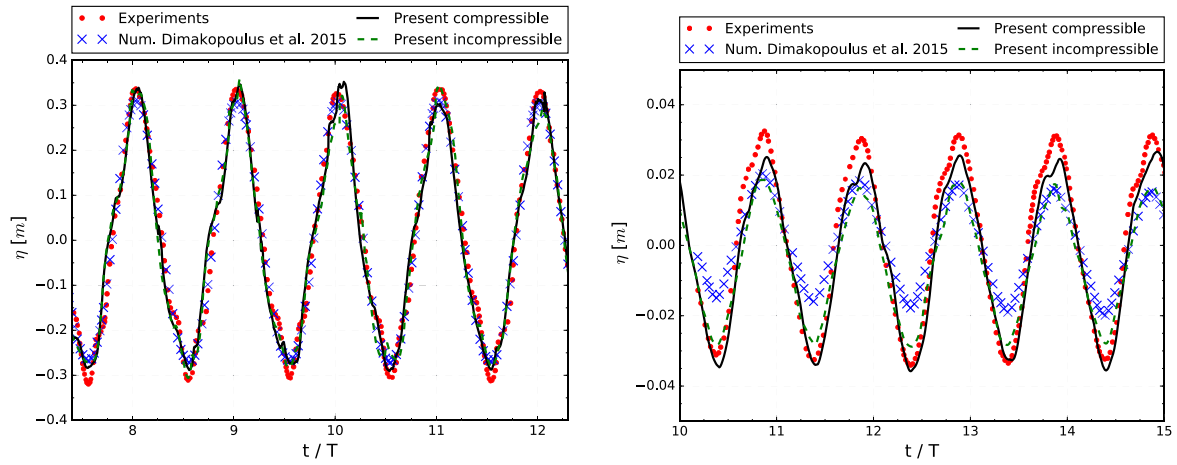

Fig. 6. In-chamber free-surface elevation averaged over three wave gauges for the two orifice openings d_0/D.

numerical results are compared with the experimental and numerical ones using an incompressible approach (Dimakopoulos et al., 2015). Under these conditions, Fig. 6 presents all these free-surface evolution. Results are just shifted in time so that the maximum elevation happens at the same instant for all the data-sets. A good agreement between the present work (black line: compressible solver and dashed green line: incompressible solver), the experiments (red points) and the work of Dimakopoulos (2015) (blue crosses) is observable on Fig. 6.

More into detail, the first configuration (test case Reg6.05 of Table 1) uses an orifice opening ratio of $d_0/D = 0.6$, where very few air compressibility effects are expected. Based in the results presented in Fig. 6(a), and as expected, differences between results issuing from compressible or incompressible solver are negligible due to the low resistance of the adjustable orifice. On the other hand, by reducing the orifice opening ratio to $d_0/D = 0.1$, air compressibility effects are now remarkable as seen on Fig. 6(b). For this $d_0/D = 0.1$ configuration, both incompressible numerical results show to provide a poor prediction of the experimentally recorded data. The present compressible solution proved to have a much more accurate prediction of the experimental measurements. However, some minor discrepancies are still noticeable. These differences are mainly due to a low mesh resolution around the tube and the chamber compared to the previous numerical results of Batlle Martin et al. (2020). The present work aims to reduce, as much as possible, the spatial and time discretisations for consistency with the incoming sections where highly computationally demanding simulations will be run. Differences with the experiments may also be explained by 3D effects to some extent.

Fig. 7 presents temporal series of pressure differences across the power take-off (PTO), being a relevant parameter for measuring the power that can be extracted from the system. Similarly as for the surface-elevation signals, these results are shifted in time with the exact same time lag extracted earlier. A positive pressure difference indicates a greater pressure inside the chamber that outside. For the lower resistance orifice, Reg06.05 configuration with $d_0/D = 0.6$, a fairly good agreement is obtained between both numerical approaches and the experiments (Fig. 7(a)), capturing the quadratic nonlinearity of the experimental signal near the zero-crossing. As mentioned before, the differences between the compressible and the incompressible solver are very little for this configuration. The pressure fluctuations are caused by some instantaneous non-realistic high velocities which may appear on singular cells due to the coarse mesh and the high-speed air flowing inside or outside the cavity close to the 90 ° air tube corners. These fluctuations do not have a direct effect on the global chamber behaviour as it is observable in the free surface evolution. The authors think that it is out of the scope of the present work to solve these numerical pressure fluctuations. Nevertheless, additional information is presented in Appendix B. Regarding the results of the orifice opening $d_0/D = 0.1$ (Fig. 7(b)), the role of air compressibility is now very distinctive. There is a phase shift between experimental records and the incompressible numerical results, both issuing from Dimakopoulos et al. (2015) or in the framework of the present study. The results obtained from the compressible numerical tends to match much more accurately with the experiments. This effect is caused by the compressibility acting like a mechanical spring in phase with the chamber free-surface elevation motion rather than the velocity. Moreover, quadratic non-linearity is also captured slightly after the air inside the chamber is fully compressed, which can be observable e.g. at $t/T \approx 10.75$ or $t/T \approx 11.75$ on Fig. 7(b). The experimental pressure data are very well reproduced by the compressible approach for this very low opening ratio $d_0/D = 0.1$.

To partially conclude, the above-mentioned results and analysis of this Section 4 gives the authors confidence to continue into more complex scenarios using random waves and the assessment of impact pressure into the curtain wall. For regular to high opening ratios (e.g. $d_0/D \geq 0.6$), the incompressible approach has proven to be largely sufficient to accurately model the inside chamber free surface elevation motion and pressure drop around the PTO. For configuration with nearly closed opening ratios (e.g. $d_0/D \geq 0.1$), the compressible approach is recommended. For the upcoming Section 5 in which impact pressure of irregular wave trains will be assessed, the considered experimental configurations are those with opening ratios $d_0/D \geq 0.4$ (Table 1). Although this precise configuration with $d_0/D = 0.4$ was not tested in the present section, it is assumed that air compressibility will not drastically modify the in-chamber flow. Therefore, the computed configuration of Section 5 will mostly consider the incompressible approach (see Table 2). Two compressible computations will be run, first for compressible / incompressible inter-comparison (Irr13.01, s=0.011) and when impulse impact events are expected (Irr11.07, s=0.030) following the findings of Batlle Martin et al. (2021). Moreover, even if the mesh resolution employed here was rather coarse, it can be concluded to be sufficient enough to properly model in-chamber phenomena.

5. Irregular waves pressures on the OWC front wall

This section is dedicated to the numerical evaluation of wave induced loads exerted by different irregular sea-states on the OWC exterior carapace. The pressure fields on the curtain wall are the result of complex wave interaction processes that enclose multiple relevant phenomena, such as:

- Generation and absorption of an irregular sea-state

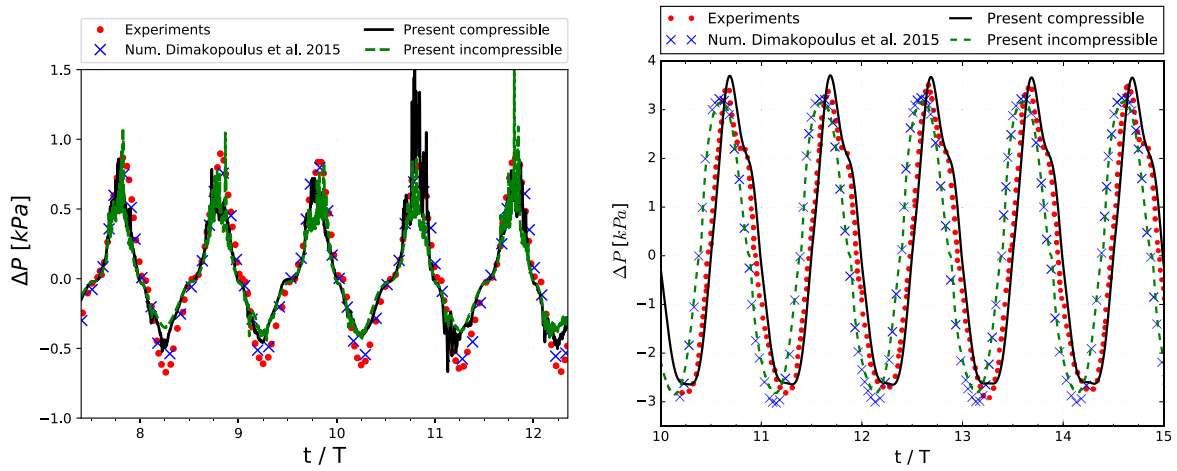

Fig. 7. Pressure difference across the adjustable orifice for the two orifice openings d_0/D.

- Wave transformation over the sloped plane
- Wave–structure interaction
- Pneumatic chamber behaviour

In a random sea environment, the assessment of a single wave event is not trivial. However, in order to have a first level of analysis, each individual wave will be detected and identified using an upcrossing method. This identification is based on an extraction from the free surface temporal series 1 m in front of the structure (wave gauge WG-08) for every single computation. Every time the free surface up-crosses the still water level, it marks the beginning of a new wave. Therefore, the wave train is divided into several individual waves, each wave has a related time interval. With this information, an interval of the pressure signal is attributed to a singular wave event. Finally, the maximum value within this pressure interval is chosen as the wave pressure value.

In order to perform a survivability analysis, the most interesting events are those related to the most energetic waves during the whole wave train. However, experience has demonstrated that the natural selection of the single maximal pressure P_{max} is too simplistic and not representative of the whole stochastic process (see e.g. Goda (2010) or Cuomo et al. (2010)). To avoid this uncertainty, the average of the pressure maxima obtained from over two hundred and fifty of the waves pressure is commonly used and denoted $P_{1/250}$. As a matter of example and for consistency with the experiments, the duration of the simulations is 1000 T_P. It means that numerical and experimental results are obtained from 1000 wave individual events and the $P_{1/250}$ is calculated using the four highest pressure values recorded.

In order to increase even more confidence in the presented results, the present study adds further perspective to the statistical nature of the selected irregular sea states by computing five times the same configuration of significant wave height, wave peak period and water depth (H_S, T_P, h). In fact, for each of the 5 identical irregular configurations, only the wave phase seed components are changed on a randomly basis. The pressure values in this section are normalised by dividing them with the hydro-static component of the significant wave height ($\rho g H_S$).

5.1. Non-impulsive conditions

In this section, two irregular sea-states, Irr01.10 and Irr13.01 (Table 1), are reproduced and compared with the experiments. The studied configurations are referred to as non-impulsive and no wave breaking is expected, although, a turbulence model is employed for a coherent comparison with the impulsive irregular situation (Section 5.2). Presumably, the most energetic wave pressures on the structure will not exceed the values of $2.5\rho g H_S$. Differences between both cases are the wave steepness and the orifice opening, which are those reproduced from the experimental study (Allsop et al., 2014). The numerical details of this configuration are presented in Table 2. The first part of the present section introduces a global convergence analysis by modifying the mesh similarly as in Appendix A. Then, the second part compares the incompressible and compressible solvers. It is important to notice the fact that the experimental pressure signals for the non-impulsive conditions are analysed using the filters detailed in Section 2.2.

Irr01.10 - ($s = 0.020$): Global convergence

The configuration evaluated in the present section has a significant wave height $H_S = 0.26$ m, a peak period $T_P = 3$ s and a water depth of $h = 3.5$ m. The physical time simulated is $1000\,T_P = 3000s$. A global convergence study is carried out in this section while comparing the experiments with numerical results using an incompressible solver for this high opening ratio $d_0/D = 0.6$ and non-impulsive wave configuration. In fact, two spatial discretisation are used, an *intermediate* referred as M2 in A and a so-called *refined* one or M3. Between the *refined* and the *intermediate* mesh, the characteristic cell length is multiplied by a factor of 3/4 leading to a new characteristic cell length of $\Delta x = 0.075$ m. The temporal discretisation is also refined by keeping the same `maxCo` = 0.4 as in the original setup.

First, Fig. 8 depicts free surface elevation spectra, one computed far from the structure over the horizontal bottom (WG-04, Fig. 8(a)), which corresponds to $l = 10$ m from Appendix A, and the other one meter in front of the OWC front wall (WG-08, Fig. 8(b)). Fig. 8(a) compares the numerical results obtained by using the two discretisations (M2 in blue and M3 in green) with the experimental data (red line) and the input spectrum (dashed black line) for the relaxation zone.

On the one hand, the input spectrum is well captured with a lower sharpening and distribution of energy towards the higher frequencies. However, these higher frequency waves are underestimated compared with the experiments and may be related to the chamber radiation phenomenon. Numerical results show convergence comparing the two obtained spectra, which are almost superposed. On the other hand, computing the spectrum in the vicinity of the structure (see Fig. 8(b)), higher discrepancies appear between the peak frequency energy from the experiments and the numerical results. The differences in the peak period spectral densities are may be related to a limited capturing of the wave reflection when using a 2D configuration compared to the 3D experimental setup, numerical dampening effects of high frequency waves, turbulence modelling or a combination of all. Still a fairly reasonable agreement is obtained and the numerical results are converged.

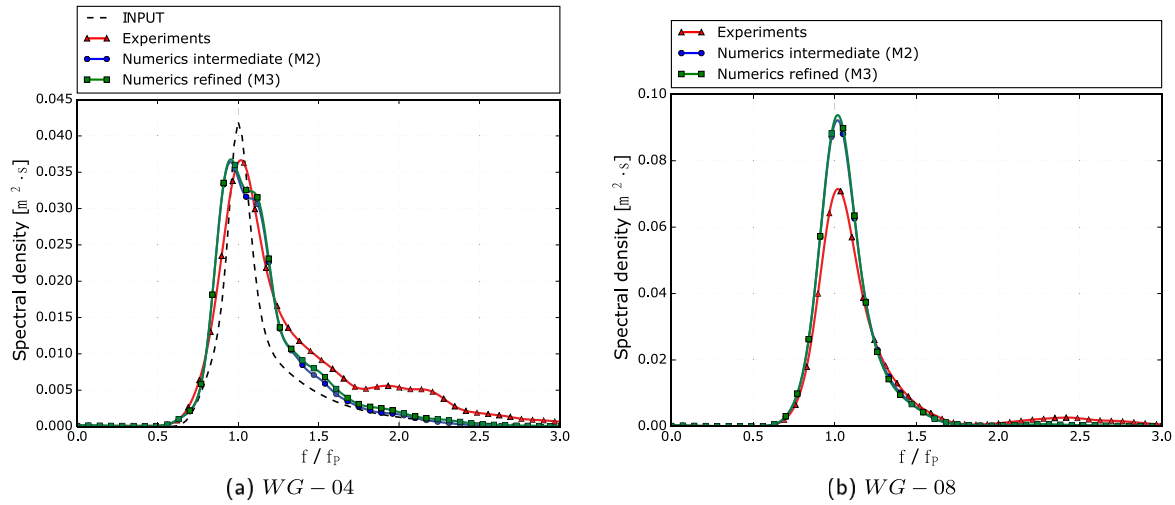

Fig. 8. Spectrum over the horizontal slope (WG-04) and one meter in front of the OWC front wall (WG-08). Test conditions (Irr01.10): $H_S = 0.26$ m, $T_P = 3$ s and $d_0/D = 0.6$.

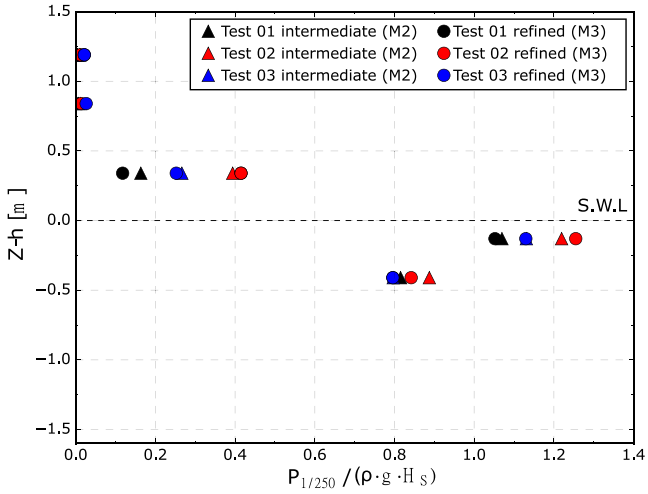

Fig. 9. Convergence of wave pressure results ($P_{1/250}$) on the structure front wall for 3 exact similar configurations using 3 different wave phase random seeds. Test conditions (Irr01.10): $H_S = 0.26$ m, $T_P = 3$ s and $d_0/D = 0.6$.

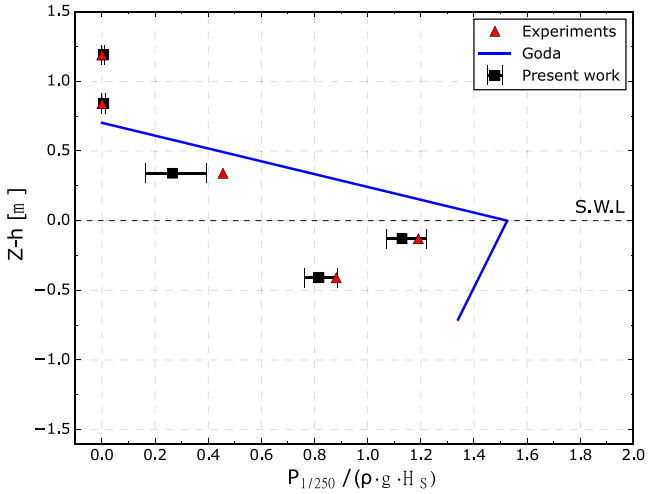

Fig. 10. Maximal adimensional wave pressure ($P_{1/250}$) ranges over 5 random seeds on the structure front wall compared with the experimental values. Test conditions (Irr01.10): $H_S = 0.26$ m, $T_P = 3$ s and $d_0/D = 0.4$.

Fig. 9 presents dimensionless pressure values at five different elevations of the OWC front wall. The location with $Z - h = 0$ corresponds to the still water level (SWL), having two immersed pressure sensors (PS 01, 02) and three above the water (PS 03, 04, 05). First, the obtained results using two discretisations are compared. Instead of five, only three runs with different phase seeds, the same ones for both discretisations, are considered for this analysis due to the high computational costs when using the refined mesh M3. Stable and converge solutions are observable between the *intermediate* and the *refined* meshes, further confirming that the *intermediate* mesh is enough when looking for reliable solutions. This *intermediate* M2 mesh is therefore selected for all the upcoming computations.

Finally, two additional computations were run with new seeds for this *intermediate* mesh. The obtained results are compared in Fig. 10 with the experiments and the prediction using Goda's formulation (Goda, 2010) for caisson breakwaters. The numerical results are represented using the average value as a black square, the range corresponding to the minimum and maximum encountered over the 5 similar computations. Comparing the results with the predictions using the pressure formulas, a relatively similar order of magnitude is encountered. The formulas proposed by Goda (2010) overpredict the values remaining on the security side, suggesting them as a good practice for design purposes. Observing the results from the experimental campaign, and the numerical results, it can be seen that they are in good agreement, from a quantitative point of view. The computed results depict the stochastic nature of the random sea with a non-negligible pressure range rather than a singular value. Furthermore, from a wider perspective, by taking into account all the statistics and analysis procedures to obtain such extreme and singular values, the authors are fairly optimistic about the computations. The computational costs for simulating 1.800 s for the present configuration ($s = 0.020$, Irr01.10) using the *intermediate* mesh M2, which has 147.000 cells, lasted for 41 h using 14 cores of an Intel Broadwell (2.4 GHz) in CRIANN (Centre Régional Informatique et d'Applications Numériques de Normandie). Even if the computational cost is not negligible, such a CFD study now starts to be affordable in pre-design or design phase of coastal engineering projects.

Irr13.01 - ($s = 0.011$)*: Compressible and incompressible comparison*

The configuration evaluated in the present section differs from the previous because of its lower wave steepness ($s = 0.011$) and smaller

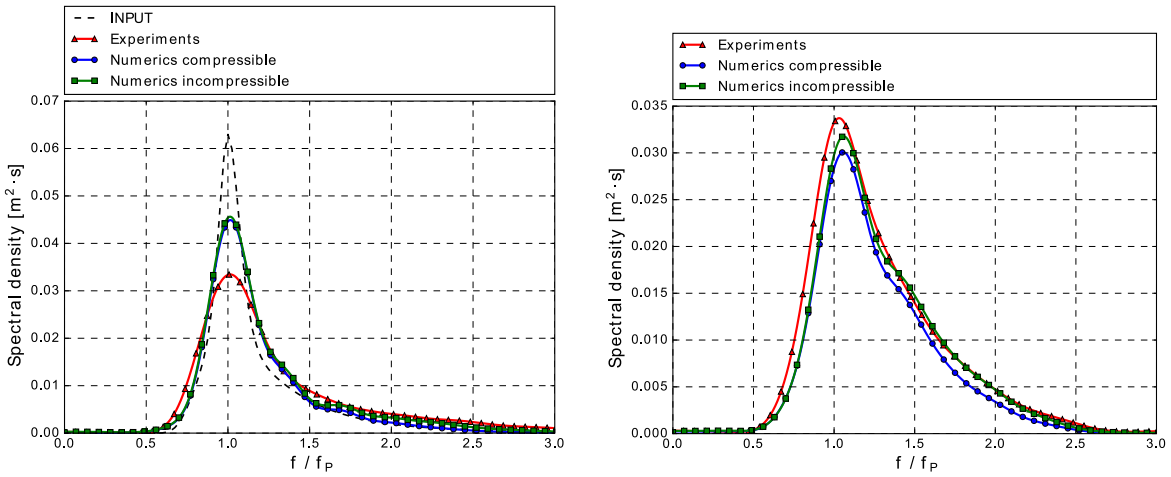

Fig. 11. Spectrum over the horizontal slope (WG-04) and one meter in front of the OWC front wall (WG-08). Test conditions (Irr13.01): $H_S = 0.26$ m, $T_P = 4.5$ s and $d_0/D = 0.4$.

opening of the orifice ($d_0/D = 0.4$). With this diameter ratio, air compressibility effects are expected to have a greater influence. In this section, the numerical results using incompressible and compressible solvers are compared with the experimental data. And for both approaches, a turbulence model is also selected for comparison with the final targeted configuration, see next Section 5.2, where wave breaking situations occur. The modified $k-\omega$ SST turbulence closure presented by Larsen and Fuhrman (2018) is available in the OpenFOAM suite for the incompressible formulation. This modified version was chosen because it proved to be more accurate and stabilise the model in nearly potential flows, limiting the growth of the turbulent kinetic energy and eddy viscosity. However, and at the time of this work, this modified $k-\omega$ SST turbulence closure model (Larsen and Fuhrman, 2018) was not yet implemented for the compressible solver (or not available); the regular $k-\omega$ SST turbulence model is used in the compressible simulations. All over the rest of the paper the regular $k-\omega$ SST turbulence model is used for compressible computations and the modified $k-\omega$ SST turbulence model (Larsen and Fuhrman, 2018) for the incompressible ones (Table 2). This may cause a slightly higher damping of the wave heights when using the compressible solver.

According to the generated spectra depicted in Fig. 11 from wave gauges (WG-04) and (WG-08), the discrepancies between the two approaches are very small. The differences due to the account of compressibility, and hence the selected turbulence model, do not seem to have an influence of the wave generation and propagation. Looking more into details to wave gauge (WG-04) located over the horizontal plane and comparing the results with the experiments and the input spectra (Fig. 11(a) right panel), discrepancies are observable. Wave reflection caused by the structure possibly reduces the energy of the spectrum peak and spreads energy into smaller wave periods, both numerically and experimentally. The numerical results differ from the experiments by keeping a sharper spectrum and, hence, slightly underestimating the energy related to smaller and higher wave periods. On the other hand, the spectra computed in the vicinity of the structure (Fig. 11(b) right panel) show a remarkably good agreement with the experiments with both numerical approaches. Nevertheless, the compressible solver slightly underestimates the energy compared with the incompressible solution, as it was hypothesised. But as a partial conclusion, both away and close to the OWC, the compressible and the incompressible solvers present very similar spectral solutions.

Fig. 12 presents results of wave induced pressure exerted on the structure curtain wall using both incompressible and compressible solvers. As in the previous case, results are represented by their averaged values combined with a range of minimum and maximum

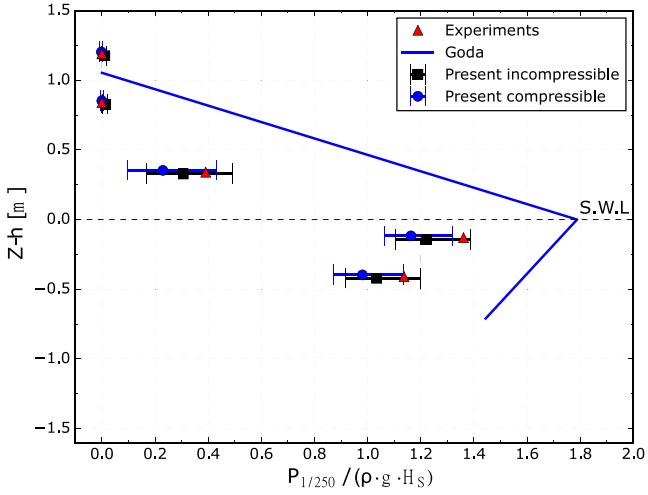

Fig. 12. Comparison of compressible and incompressible maximal dimensionless wave pressure results ($P_{1/250}$) on the structure front wall evaluated over 5 computations with different phase random seeds. Test conditions (Irr13.01): $H_S = 0.26$ m, $T_P = 4.5$ s and $d_0/D = 0.4$.

values obtained over 5 identical computations. In this context, predictions using the (Goda, 2010)'s formulation again over-predict the experimental values by an offset of $0.4\rho g H_S$. Both the incompressible and compressible solutions have a fairly good agreement with the experiments. It is also observable the statistical nature of the maximal pressure values related to the same sea-state with ranges of pressure rather than a single value. The compressible and incompressible results have a very similar trend, although the compressible solver presents a higher diffusion as expected, and slightly reduces the pressure ranges and maximum values.

To conclude, both incompressible and compressible solvers have demonstrated stability and accuracy when solving these two non-impulsive configurations with reasonably high opening ratios ($d_0/D \geq 0.4$). Both solvers also proved to be accurate when handling very large stochastic processes.

5.2. *Impulsive conditions* - ($s = 0.030$)

This section presents the results obtained using a new irregular sea state configuration (Irr11.07, $s = 0.030$). During the experimental tests, this configuration produced multiple wave breaking with high

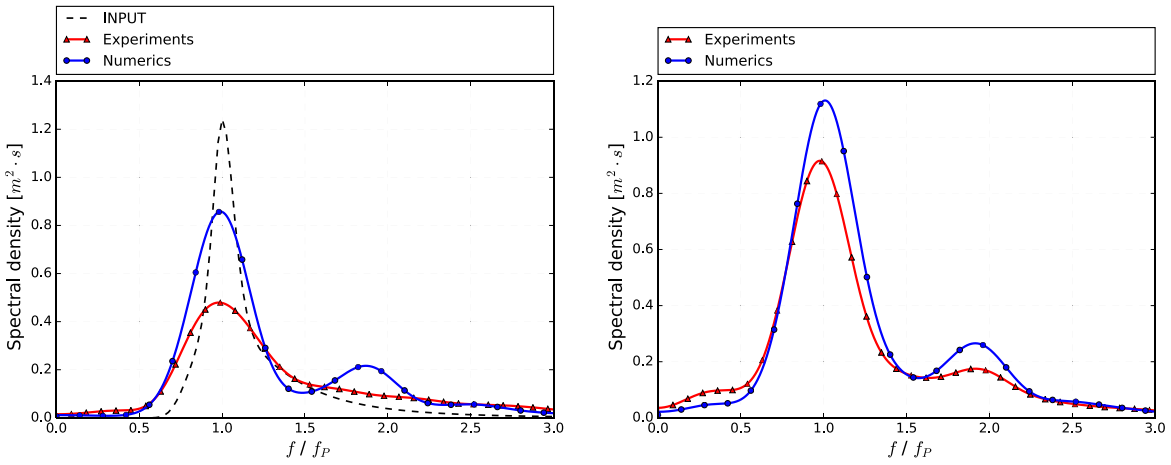

Fig. 13. Spectrum over the horizontal slope (WG-04) and one meter in front of the OWC front wall (WG-08). Test conditions (Irr11.07): $H_S = 1$ m, $T_P = 6$ s and $d_0/D = 0.4$.

energetic loads classified as impulsive (Allsop et al., 2014). To study these conditions, analysis using the variable $P_{1/250}$ are less representative due to the high variability of the pressure maxima related to the most energetic impacts. Therefore the analysis is here limited to some selected singular events and their pressure signals. In fact, the presented computations were computationally very expensive due to high velocities for wave breaking. The free surface refinement region has been increased vertically in order to maintain the interface within its limits owing to a much higher H_s value. Consequently, due to the increase in the number of mesh cells and especially the smaller time steps, the physical time for these simulations was limited to $1000\,T_P/3 = 2000\,s$. The same set of five different phase seeds runs are kept for this irregular sea state conditions.

The numerical details for this configuration are presented in Table 2. Following the conclusions of Batlle Martin et al. (2021) (or Lu et al. (2021) using another numerical approach) incompressible formulations proved to generate spurious and non-physical impact pressures when impulsive events are considered. Only a compressible formulation can give accurate results as shown in Batlle Martin et al. (2021). Therefore, only the compressible formulation was used for this configuration.

Fig. 13 presents the spectrum over the horizontal slope (WG-04) and 1 m in front of the structure (WG-08). It is important to notice here the lower physical time of the present simulations which may affect the sea state long term development. Hence, the computed spectrum over the horizontal slope (WG-04) presents visible discrepancies with the experiments. From Fig. 13(a), a generalised overestimation of energy is noticeable from the numerical results compared with the experiments. The experimental higher frequencies $f > f_P$ are equally distributed while the numerical ones are grouped around some characteristic values mainly around $f/f_P \approx 1.9$ and to some lower extent at $f/f_P \approx 2.5$. Also, energy in the infragravity bond ($T > 30s$) can be presumably identified from the experimental spectrum. These are underestimated in the numerics over the horizontal plane (WG-04, Fig. 13(a)). Regarding the spectrum in the vicinity of the structure (WG-08, Fig. 13(b)) a fairly good agreement is obtained in terms of shape between the numerics and the experiments. Similar analyses as the ones observed for (WG-04) can be made with a general numerical overestimation of the energy related to the peak period and higher frequency waves. Also, the presence of energy for long period waves has increased in the numerical solution compared to (WG-04), however, the experimental values keep being underestimated. A preliminary observation can be extracted from this analysis, which points towards a lower presence of wave breaking effects due to a smaller representation of long-period waves. The overall agreement regarding the energy distribution and density

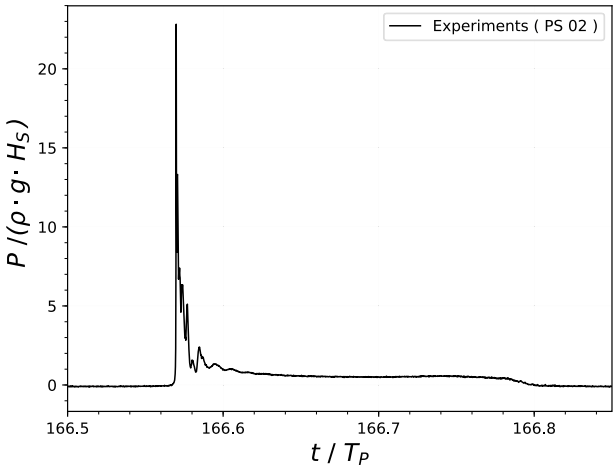

Fig. 14. Experimental pressure signal, from Allsop et al. (2014), recorded by wall pressure transducer (PS 02) on the exterior front wall for a impulsive event. Test conditions (Irr11.07, $s = 0.030$): $H_S = 1$ m, $T_P = 6$ s and $d_0/D = 0.4$.

gives confidence about the numerical conclusions, because of the fact that these are not numerical artifacts and more generally that the presented computations accurately represent the physical encountered phenomena.

When looking at the wall pressure temporal series, the experiments presented an extreme situation (Fig. 14), where the pressure peaks exceeded 20 times the significant wave height hydro-static pressure. These impacts are typical of plunging waves with rise time values around $t_r \approx 0.001T_P$. Unfortunately, not a single similar event could be numerically captured, where the maximal pressure values were always below 3 times the significant wave height pressure head. This further confirms the observation extracted from the computed spectrum meaning that not any real plunging breaker encountering the OWC front wall occurred during the simulations. However, Batlle Martin et al. (2021) have successfully reproduced very impulsive impacts using OpenFOAM, either in 2D or 3D for the case of a single solitary wave impinging a wall. The reasons for this non-appearance of plunging breakers here are still unknown although the authors believe that several aspects play an important role in these conclusions: the 3D configuration of the experiments leading to different behaviour of the chamber oscillations, the low discretisation adopted for a feasible computational cost objective, slight differences in the irregular sea state

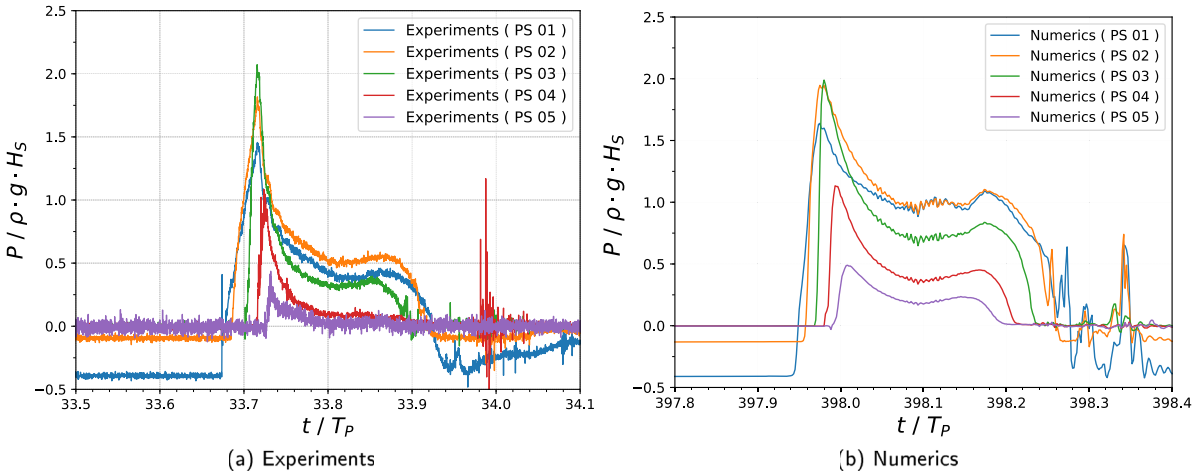

Fig. 15. Comparison of experimental and numerical pressure signal recorded by wall pressure transducer (PS 02) on the exterior front wall for a violent wave impact. Test conditions (Irr11.07): $H_S = 1$ m, $T_P = 6$ s and $d_0/D = 0.4$.

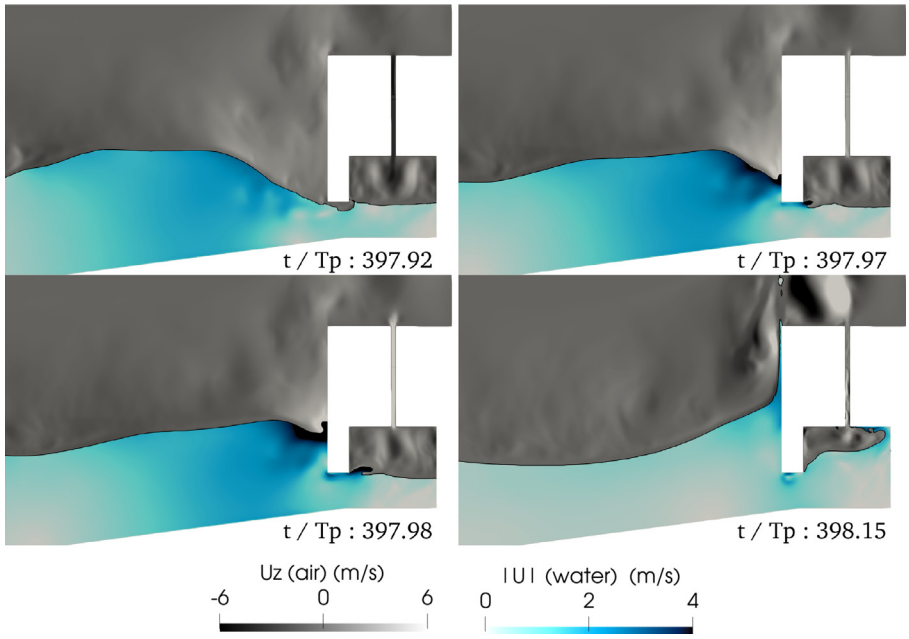

Fig. 16. Snapshots of velocity magnitude for water and vertical velocity for air, for four relevant instants during a wave impact, pressure signal Fig. 15(b).

displacing the breaking point or a too coarse definition of the free surface profile avoiding overturning configurations.

Nevertheless, some lower order of magnitude violent wave–structure impacts are observed on the numerical pressure sensors as depicted in Fig. 15. Pressure signals related to this type of phenomena reach values up to $2\rho g H_s$ and have an approximate rise time of $t_r \approx 0.01 T_P$, which is one order of magnitude higher than those from the extreme impact loads. They present the classic double-peaked or 'church roof' shape related to the initial impact, deflection and reflection of the wave. The sudden pressure rise indicates an important role of the fluid deceleration in this wave interaction with the structure. In Fig. 15 both numerical and experimental events are selected randomly from the pressure signals and it is observable a clear resemblance between numerical and experimental impulsive events.

For a better understanding of the pressure peak caused by an incident impact of the wave against the structure, four relevant instants are presented in Fig. 16. In the first image (t/T = 397.92), a reflected and an incoming wave are superposed in front of the structure. The free surface inside the OWC chamber is falling sucking in air from the exterior. The bottom lip of the OWC curtain wall is not submerged. This is an unexpected situation and, in principle, should be avoided for a correct functioning of the OWC. Next (t/T = 397.97), the front wall bottom lip is exposed to a fluid impact originating two water tips, one travelling upwards from the front wall and, a second one, towards the chamber rear wall. The velocities of these tips are non-negligible with values up to 5 m/s. The incoming wave starts loading the bottom part of the front wall further accelerating the rising water tongue. At (t/T = 397.98), the pressure signal presented in Fig. 15(b) reaches its maximum and the incoming wave fully charges the vertical wall. The front wall is fully charged from the exterior side and remains only surrounded by the air from the interior side, causing an important bending moment. The chamber is now pushing the air outwards. In the last snapshot (t/T = 398.15), the deflection and reflection stage of the wave is observable where the fluid is fully projected upwards forming some water independent small structures which are captured by the simulation. Under the front wall bottom lip, a vortical structure appears again. Inside the chamber, the liquid undergoes a sloshing type situation leading to some impacts with the interior walls and fully

compressing the air. These were also observed during the experimental tests, see Pawitan et al. (2020), and may cause unexpected damages if not addressed properly.

6. Conclusion

This paper presents a numerical investigation of real large scale oscillating water column (OWC) structure facing nearshore sea state. The main objective of this paper being to investigate the possibility of assessing extreme wave loads caused by random waves on an OWC device using a CFD tool, the presented results have demonstrated important steps towards this final objective by direct comparison of numerical and experimental data.

First, the generation and propagation of regular and irregular wave fields using a relaxation zone technique is evaluated, also with the addition of the sloping beach and OWC structure on one side of the flume. A good convergence of the wave height is presented for regular waves and a good spatial discretisation convergence of the zeroth momentum spectral wave height is presented for irregular waves. Different irregular sea states using the JONSWAP spectrum based on various wave steepness ($s = H_s/\lambda_p$) have been tested and a mesh sensitivity analysis has been carried out observing the influence of the spatial discretisation on both the generation and propagation of irregular waves. Maintaining the same mesh for all the configuration, it has been observed a better reproduction of the smaller steepness cases. A higher conservation of the spectral energy is obtained while refining the spatial discretisation. Moreover, the higher relative depth configuration (closer to deep water conditions) presented the higher generation errors. Finally, the apparition of a second frequency harmonic has been observed for the higher steepness configuration ($s = 0.03$) showing that the solver could capture accurately physical phenomena (high steepness and the presence of the OWC structure).

Next, the in-chamber complex flow motion was assessed with the OWC facing regular waves as experimentally studied by Allsop et al. (2014). The experimental device being equipped with a PTO system, was modelled here using a porous medium approach. Following the experimental configurations, two different configurations have been tested with different opening ratios of the devices. This was taken into account in the numerics by changing the porous medium airflow resistance and a remarkably good agreement has been observed when compared with the experiments. The highest resistances (low opening ratio) have shown that taking the air as incompressible leads to erroneous results, as already pointed out by Dimakopoulos et al. (2015), and a compressible approach is needed. Regarding the pressure gradient around the modelled PTO and the in-chamber free-surface motion, the compressible solver has been able to accurately capture the compressibility effects observed experimentally.

The present work also compares the numerical and experimental results of three different irregular sea states acting on an oscillating water column. The experimental configurations and results from Allsop et al. (2014), Pawitan et al. (2019, 2020) were used here as a matter of validation. The free surface elevation spectra computed far from the structure and in front of the structure presented a fairly good agreement for the two irregular configurations classified as non-impulsive ($s \leq 0.02$). A global sensitivity analysis was carried out for one irregular sea state configuration and converged results were observed for the spectrum and the extreme pressures ($p_{1/250}$) exerted on the OWC front wall on this non-impulsive configuration. Moreover, using another non-impulsive irregular sea-state configuration with a smaller opening ratio ($d_0/D = 0.4$) to possibly highlight differences, the compressible and incompressible solvers have been compared. And very similar results were obtained (for both free-surface elevation, impact pressure), although the compressible solver presented higher energy dissipation with lower extreme pressure ranges. The extreme pressure ($p_{1/250}$) exerted on the OWC front wall highlighted the stochastic nature of the irregular sea-state and presented a range of solutions in good accuracy with the experimental results (Pawitan et al., 2019). The extreme pressure experimental values have been successfully validated for two non-impulsive irregular sea state configurations and the paper's objective is validated so far.

Finally, more energetic irregular sea-state with breaking waves acting on the OWC is investigated, closer to a stormy condition. Such a configuration is really interesting in terms of survivability assessment. The computed spectra far and near to the structure have shown resemblances with the experiments. However, the numerical results underestimated the long period waves energy and, far from the structure, a narrower peak is obtained. But, the second harmonic is also numerically captured in accordance with the experiments even though the level of energy is not well reproduced. With respect to impact pressures, only the compressible solver was selected for this impulsive case as incompressible solvers have shown important inaccuracies in previous studies (Batlle Martin et al., 2021; Lu et al., 2021). The most energetic wave impacts during the experiments were not observed in the numerical simulations. This might be caused by different reasons such as: slight differences in the sea state parameters, 3D effects during the experiments, the necessity of finer temporal and spatial resolution, the turbulence model. Definitive conclusions from this impulsive loads section would need further investigations. However, promising results are already observed and a general optimistic perspective can be extracted as accurate impulsive impacts were already computed by Batlle Martin et al. (2021), with higher computational costs not yet affordable in such a stochastic configuration as the one presented here.

To conclude, numerical computations of a large scale OWC facing different wave conditions using a 2D configuration were presented and successfully validated against experiments. This work states that if one wants to accurately reproduce an OWC in-chamber complex flow motion for all the range of PTO operating points, a compressible solver is needed.

CRediT authorship contribution statement

Marc Batlle Martin: Software, Validation, Formal analysis, Investigation, Writing – original draft. **Grégory Pinon:** Conceptualization, Validation, Formal analysis, Investigation, Resources, Writing – review & editing, Supervision, Funding acquisition. **Gabriel Barajas:** Formal analysis, Investigation, Resources, Writing – review & editing. **Javier L. Lara:** Formal analysis, Investigation, Resources, Writing – review & editing. **Julien Reveillon:** Formal analysis, Investigation, Writing – review & editing, Supervision, Funding acquisition.

Declaration of competing interest

The authors declare that they have no known competing financial interests or personal relationships that could have appeared to influence the work reported in this paper.

Data availability

The experimental data is part of the Hydralab IV project.

Acknowledgements

M. Batlle Martin acknowledges the financial support for his PhD grant from the regional council of Normandie. The authors acknowledge the financial support of the CPER-ERDF program DIADEMAR funded by the Upper Normandy Regional Council and the European Union. The present work was performed on computing resources provided by CRIANN (Normandy, France). The authors acknowledge the financial support of the Agence Nationale de la Recherche, through the program Investissements d'avenir - LabEx EMC3 via the project PERCUSS. The authors would like to acknowledge the "HyIV-FZK-02" project, for providing all the raw recorded files from the aforementioned experimental campaign and especially Prof. D. Vicinenza and Prof. M. Kudella for their help and explanations.

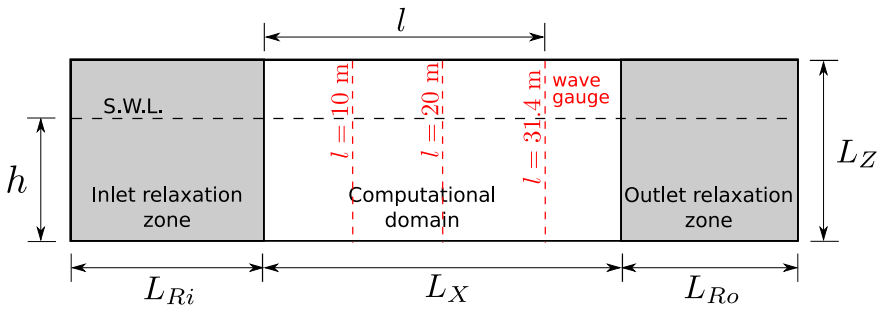

Fig. 17. Geometrical definition of the numerical wave tank.

Table 3
Numeric wave tank dimensions.

L_{Ri} (m)	50
L_{Ro} (m)	20
L_X (m)	40
L_Z (m)	6

Appendix A. Convergence study for the generation and propagation of regular and irregular sea states

This appendix section is dedicated to the validation of the relaxation zone method for the generation and propagation of the considered wave conditions. It also indicates the spatial and temporal discretisation required to reproduce a target wave conditions over a flat plane.

For this purpose, a simple rectangular numerical wave tank (NWT) in 2D (see Fig. 17) is used to generate, propagate and absorb regular and irregular waves. The numerical wave tank geometrical characteristics are summarised in Table 3 where L_{Ri}, L_{Ro} stands for the inlet and outlet relaxation zone length, L_X the computational domain length, L_Z the domain height, h the water depth and $S.W.L.$ the still water level. The top boundary is defined as open boundary with a total pressure where air and water can freely flow out and only air can flow in. The bottom boundary is defined as a solid wall with a no-slip condition; the inlet and outlet boundaries have the prescribed velocity and free surface elevation conditions given by the relaxation zone method. All over the domain, a structured grid is used with a cell aspect ratio of $\Delta x/\Delta z = 1$. Additionally, around the free surface, a refined region is defined where the cell sizes are divided by two. Three different spatial discretisations (M1, M2, M3) are employed using a refinement factor of 4/3. The resultant number of cells ratios per significant wave height $H_s/\Delta z$ or wavelength $\lambda_p/\Delta z$ are presented in Table 4. Before a discussion of the results from the simulations, it is important to highlight the relatively coarse spatial and temporal discretisation to evaluate the limit of both accuracy and time consumption for large stochastic simulations. These simulations are performed using the incompressible solver and the modified $k-\omega$ SST turbulence model.

Wave parameters are presented in Table 2. Three numerical wave gauges ($L1, L2, L3$) were located respectively, $l = 10$ m, $l = 20$ m and $l = 31.4$ m away from the end of the relaxation zone inlet region and recorded the free surface variations every 0.1 s. These distances correspond (based on the validation geometry Section 3.2) to: half of the distance between the end of the relaxation zone and the beginning of the sloped plane ($L1$), the beginning of the sloped plane ($L2$) and the OWC front wall ($L3$). Regarding the irregular waves conditions, spectra is calculated using the Welch's method (Welch, 1967) from the temporal series and compared with the input spectrum.

Fig. 18 presents the obtained results for three irregular configurations (irr13.01, irr01.10, irr11.07) and three different discretisations (M1, M2, M3). It is observable a fairly good convergence of the obtained spectral density towards the input spectrum while reducing the discretisation errors for all three configurations. The best agreements are obtained in the wave gauge close to the inlet boundary (L1) and there is a general dissipation of energy further away from the generation zone caused by numerical damping.

The lower steepness configuration ($s = 0.011$) presents a very good agreement with the input spectrum in terms of distribution and magnitude and very low energy dissipation while propagating. On the other hand, the intermediate steepness case presents a reasonably good agreement with the input spectrum regarding the peak frequency energies, although, it tends to underestimate the higher frequencies. These differences may come from the fact that this configuration has the highest relative depth ($h/\lambda_P \approx 0.27$) and the lowest mesh resolution. Finally, the highest steepness configuration presents the lower overall agreement with the input spectra when observing the peak frequency and higher frequencies related energy. It is expected that steep waves experience more numerical damping and also possibly due to wave breaking during the propagation. In contrast with the general trend for this configuration, the peak frequency energies are lower at L2 than in L3 and they are apparently displaced to higher frequencies localised around a second frequency harmonic. These are most likely produced by the effect of reflection from the boundaries.

Fig. 19 presents the spectrum zeroth momentum wave height $H_{m0} = 4\sqrt{m0}$ relative errors $Err(H_{m0}) = (H_{m0}^{input} - H_{m0})/H_s^{input}$ compared with the input H_{m0}^{input}. The dissipation rate of energy during the waves propagation is apparently the same when using the three discretisations for all the irregular configurations (see Fig. 19(a) left panel). Regarding the results for the first configuration ($s = 0.011$, Irr13.01), the previous analysis is further confirmed with differences for the zeroth momentum wave height around 1% for the first gauge (L1, $l = 10$ m) on all three discretisations and a final difference of $\approx 3\%$ for (M2–M3) and $\approx 6\%$ for M1 for the last gauge (L3, $l = 31.4$ m). The second configuration ($s = 0.020$, Irr01.10) presents the highest differences at the vicinity of the wave generator and the highest energy dissipation throughout the NWT. These is mainly caused because of a lower refinement (Table 4) and the higher relative depths. Finally, the third irregular configuration (($s = 0.030$), Irr11.07) present overall differences below 5% using the finest meshes (M2-M3) and a higher numerical dissipation with 7% using the coarser mesh (M1) at the last wave gauge (L3). From these results, M2 is the most suitable option for balancing accuracy and computational costs.

A similar analysis for the regular waves (Reg6) is presented in Fig. 19(b) (left panel), where the numerical wave height is extracted directly from the free surface elevation and averaged over 15 waves at the different locations. The differences at L1 remain below 5% for the three discretisations and the wave height are reduced a 10% at the last wave gauge (L3) when using the coarser mesh (M1), as expected.

This appendix has covered one regular and three different irregular sea state configurations evaluating the generation and propagation accuracy using various discretisations. Affordable computational times for very long simulations was one of the objectives of the present section and this is the main reason why fairly coarse discretisations are employed. The computational costs varied for each configuration. But, as a matter of example, the simulation of 4 500 s of physical time for

Table 4
Spatial discrestisation details.

	*Irr*13.01			*Irr*01.10			*Irr*11.07			*Reg*6		
Hs/λ	0.011			0.020			0.030			0.020		
	M1	M2	M3	M1	M2	M3	M1	M2	M3	M1	M2	M3
$H_s/\Delta z$	4	5	7	4	5	7	15	20	26	6	8	11
$\lambda_p/\Delta z$	349	466	621	196	262	349	493	657	876	300	400	533
N° cells	185k	211k	388k	185k	211k	388k	185k	334k	619k	185k	211k	388k

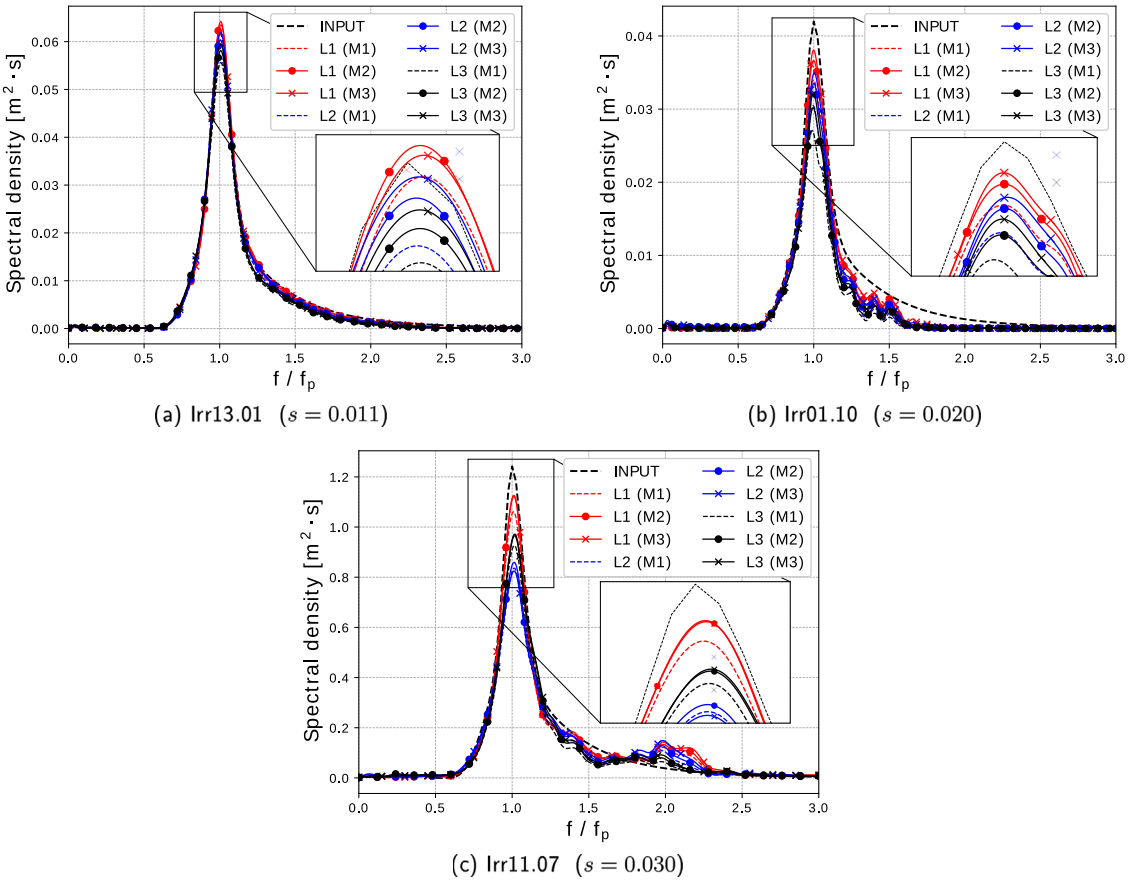

Fig. 18. Spectral analysis of different simulated irregular sea states compared with the input spectrum following a JONSWAP calibration. The spectrum's are obtained for three different meshes (M1, M2, M3) at three locations L1, L2 and L3.

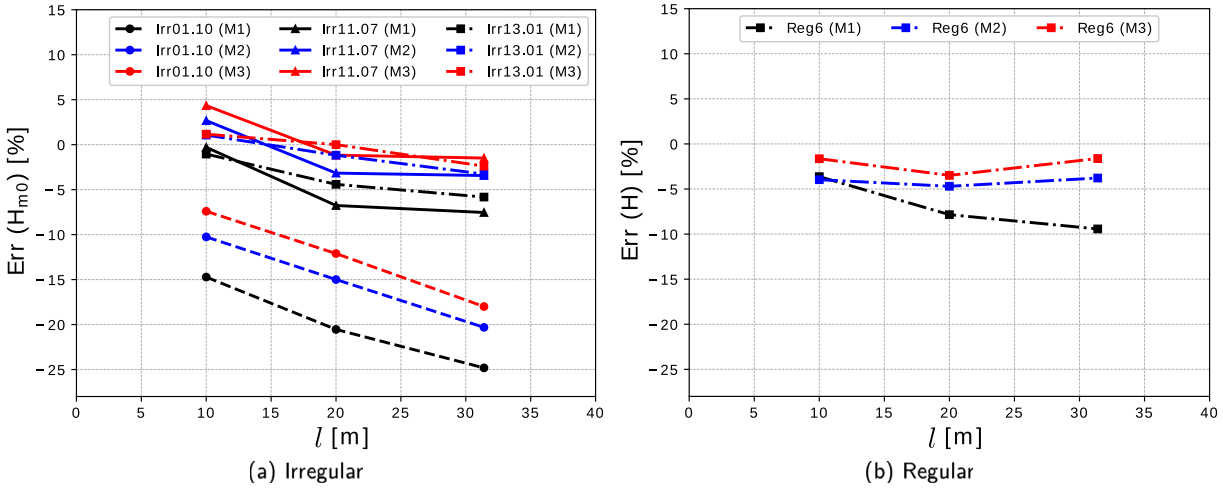

Fig. 19. Wave height relative errors using different discretisations (M1, M2, M3) along the NWT for three irregular waves configurations (Irr01.10, Irr11.07, Irr13.01) (left panel) and regular waves (right panel). The results are obtained at three locations (L1, L2, L3).

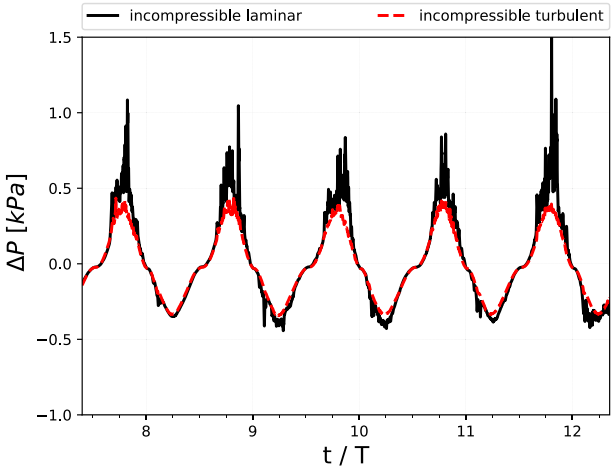

Fig. 20. Pressure difference across the OWC adjustable orifice ($d_0/D = 0.6$) using a laminar and a turbulence model.

the lower steepness ($s = 0.011$, Irr13.01) using the intermediate mesh (M2), which has 213.000 cells, lasted for 23 h, using 28 cores of an Intel Broadwell (2.4 GHz) in CRIANN (Centre Régional Informatique et d'Applications Numériques de Normandie). One may conclude that a good performance of the generation method under these conditions is achieved and that a fairly good accuracy for propagation over reasonable length has been observed.

Finally, in other Sections (4 and 5), the propagation lengths are in range with this study and the selected discretisations is M2 (see Table 4) for all the presented simulations. The presented convergence analysis study comforted us in the fact the input wave characteristics are well reproduced and propagated over the whole length of the considered geometry. Also, the use of such a mesh enables the computation of several runs of the same configuration in order to perform a statistical analysis with reasonable computational time.

Appendix B. OWC air flow modelling

The modelisation of a highly accelerated fluid through a tube entry/exit with 90 ° corners is a common cause of numerical instabilities for CFD models. In the present framework, this situation is observable in Fig. 7(a), Section 4, when the adjustable orifice of the OWC offers small resistance and the air accelerations are higher.

As presented in the next Fig. 20, by using a turbulence model (here $k - \omega$ SST) one can improve the stabilisation of the fluctuations to a certain extent, because velocities are smoothed, but the numerical issue remains.

References

Allsop, W., Bruce, T., Alderson, J., Ferrante, V., Russo, V., Vicinanza, D., Kudella, M., 2014. Large scale tests on a generalised oscillating water column wave energy converter.

Anand, S., Jayashankar, V., Nagata, S., Toyota, K., Takao, M., Setoguchi, T., 2007. Performance estimation of bi-directional turbines in wave energy plants. J. Therm. Stresses http://dx.doi.org/10.1007/s11630-007-0346-1.

Bagnold, R.A., 1939. Interim report on wave-pressure research, (includes plates and photographs). J. Inst. Civ. Eng. 12, 202–226. http://dx.doi.org/10.1680/ijoti.1939.14539.

Batlle Martin, M., Pinon, G., Reveillon, J., 2020. Numerical assessment of wave induced loads on an oscillating water column carapace. In: Taylor, Group F (Ed.), Developments in Renewable Energies Offshore: Proceedings of the 4th International Conference on Renewable Energies Offshore. http://dx.doi.org/10.1201/9781003134572.

Batlle Martin, M., Pinon, G., Reveillon, J., Kimmoun, O., 2021. Computations of soliton impact onto a vertical wall: Comparing incompressible and compressible assumption with experimental validation. Coast. Eng. 164, 103817. http://dx.doi.org/10.1016/j.coastaleng.2020.103817, https://www.sciencedirect.com/science/article/pii/S0378383920305032.

Bullock, G., Obhrai, C., Peregrine, D., Bredmose, H., 2007. Violent breaking wave impacts, Part 1: results from large-scale regular wave tests on vertical and sloping walls. Coastal Eng. 54, 602–617. http://dx.doi.org/10.1016/j.coastaleng.2006.12.002.

Cole, R.H., 1948. Underwater Explosions. Princeton Univ. Press, Princeton.

Cooker, M.J., Peregrine, D.H., 1990. Violent Water Motion at Breaking-Wave Impact. pp. 164–176. http://dx.doi.org/10.1061/9780872627765.014.

Cuomo, G., Allsop, W., Bruce, T., Pearson, J., 2010. Breaking wave loads at vertical seawalls and breakwaters. Coastal Eng. 57, 424–439. http://dx.doi.org/10.1016/j.coastaleng.2009.11.005.

de Rouville, A., Besson, P., Petry, P., 1938. État actuel des études internationales sur les efforts dus aux lames.

Deshpande, S.S., Anumolu, L., Trujillo, M.F., 2012. Evaluating the performance of the two-phase flow solver interFoam. Comput. Sci. Discov. 5, 014016. http://dx.doi.org/10.1088/1749-4699/5/1/014016.

Dimakopoulos, A., Cooker, M., Medina-Lopez, E., Longo, D., Pinguet, R., 2015. Flow characterisation and numerical modelling of owc wave energy converters.

Elhanafi, A., Fleming, A., Macfarlane, G., Leong, Z., 2017. Numerical hydrodynamic analysis of an offshore stationary–floating oscillating water column–wave energy converter using cfd. Int. J. Nav. Archit. Ocean Eng. 9, 77–99. http://dx.doi.org/10.1016/j.ijnaoe.2016.08.002, https://www.sciencedirect.com/science/article/pii/S2092678216304290.

Falcã A.F. Sarmento, A.J., Gato, L.M., Brito-Melo, A., 2020. The pico owc wave power plant: Its lifetime from conception to closure 1986–2018. Appl. Ocean Res. 98, 102104. http://dx.doi.org/10.1016/j.apor.2020.102104.

Goda, Y., 2010. Random Seas and Design of Maritime Structures, third ed. World Scientific, http://dx.doi.org/10.1142/7425, http://arxiv.org/abs/https://www.worldscientific.com/doi/pdf/10.1142/7425.

Hattori, M., Arami, A., Yui, T., 1994. Wave impact pressure on vertical walls under breaking waves of various types. Coast. Eng. 22, 79–114. http://dx.doi.org/10.1016/0378-3839(94)90049-3, special Issue Vertical Breakwaters.

He, F., Huang, Z., 2016. Using an oscillating water column structure to reduce wave reflection from a vertical wall. J. Waterw. Port Coast. Ocean Eng. 142, 04015021. http://dx.doi.org/10.1061/(ASCE)WW.1943-5460.0000320.

Higuera, P., Lara, J.L., Losada, I.J., 2013. Realistic wave generation and active wave absorption for navier–stokes models: Application to openfoam®. Coast. Eng. 71, 102–118. http://dx.doi.org/10.1016/j.coastaleng.2012.07.002.

Iturrioz, A., Guanche, R., Lara, J., Vidal, C., Losada, I., 2015. Validation of openfoam®for oscillating water column three-dimensional modeling. Ocean Eng. 107, 222–236. http://dx.doi.org/10.1016/j.oceaneng.2015.07.051, https://www.sciencedirect.com/science/article/pii/S0029801815003649.

Jacobsen, N.G., Fuhrman, D.R., Fredsøe, J., 2012. A wave generation toolbox for the open-source cfd library: Openfoam®. Internat. J. Numer. Methods Fluids 70, 1073–1088. http://dx.doi.org/10.1002/fld.2726.

Jarlan, G., 1961. A perforated vertical wall breakwater. Dock Harb. Auth. 394–398.

Larsen, B.E., Fuhrman, D.R., 2018. On the over-production of turbulence beneath surface waves in reynolds-averaged navier–stokes models. J. Fluid Mech. 853, 419–460. http://dx.doi.org/10.1017/jfm.2018.577.

Lu, X., Cherfils, J.M., Pinon, G., Rivoalen, E., Kimmoun, O., Brossard, J., 2021. SPH numerical computations of wave impact onto a vertical wall with experimental comparisons. C. R. Méc. 349, 117–143. http://dx.doi.org/10.5802/crmeca.72, https://hal-normandie-univ.archives-ouvertes.fr/hal-03167882.

Medina-Lopez, E., Allsop, W., Dimakopoulos, A., Bruce, T., 2015. Conjectures on the Failure of the OWC Breakwater at Mutriku. pp. 592–603. http://dx.doi.org/10.1061/9780784480304.063.

Miller, D., 1978. Internal flow systems.

Neumann, F., Crom, I.L., 2011. Pico owc - the frog prince of wave energy? recent autonomous operational experience and plans for an open real-sea test centre in semi-controlled environment. In: 9th European Wave and Tidal Energy Conference. EWTEC, Southampton, UK.

Oumeraci, H., Allsop, W., Groot, M., Crouch, R., Vrijling, J., Kortenhaus, A., Voortman, H., 2001. Probabilistic Design Tools for Vertical Breakwaters. Technical Report.

Pawitan, K.A., Dimakopoulos, A.S., Vicinanza, D., Allsop, W., Bruce, T., 2019. A loading model for an owc caisson based upon large-scale measurements. Coast. Eng. 145, 1–20. http://dx.doi.org/10.1016/j.coastaleng.2018.12.004.

Pawitan, K.A., Vicinanza, D., Allsop, W., Bruce, T., 2020. Front wall and in-chamber impact loads on a breakwater-integrated oscillating water column. J. Waterw. Port Coast. Ocean Eng. 146, 04020037. http://dx.doi.org/10.1061/(ASCE)WW.1943-5460.0000595.

Shigeo Takahashi, K.T., ichiro Shimosako, K., 1993. Experimental Study of Impulsive Pressures on Composite Breakwaters -Fundamental Feature of Impulsive Pressure and the Impulsive Pressure Coefficient. Technical Report.

Stevenson, T., 1840. The design and construction of harbours: A treatise on maritime engineering. In: Cambridge Library Collection - Technology. Cambridge University Press, http://dx.doi.org/10.1017/CBO9780511997020.

Suzuki, M., Arakawa, C., Takahashi, S., 2004. Performance of wave power generating system installed in breakwater at sakata port in Japan.

Takahashi, S., 1988. Hydrodynamic characteristics of wave-power-extracting caisson breakwater. Coastal Eng. Proc. 1 (185), http://dx.doi.org/10.9753/icce.v21.185, https://icce-ojs-tamu.tdl.org/icce/index.php/icce/article/view/4392.

Takahashi, S., Tanimoto, K., Miyanaga, S., 1985. Uplift wave forces due to compression of enclosed air layer and their similitude law. Coastal Eng. Jpn. 28, 191–206. http://dx.doi.org/10.1080/05785634.1985.11924415.

Torre-Enciso, Y., Ortubia, I., de Aguileta, L.L., Marqués, J., 2009. Mutriku wave power plant: from the thinking out to the reality. In: 8th European Wave and Tidal Energy Conference. EWTEC, Uppsala, Sweden.

Vicinanza, D., Lauro, E.D., Contestabile, P., Gisonni, C., Lara, J.L., Losada, I.J., 2019. Review of innovative harbor breakwaters for wave-energy conversion. J. Waterw. Port Coast. Ocean Eng. 145, 03119001. http://dx.doi.org/10.1061/(ASCE)WW.1943-5460.0000519.

Viviano, A., Musumeci, R.E., Vicinanza, D., Foti, E., 2019. Pressures induced by regular waves on a large scale owc. Coast. Eng. 152, 103528. http://dx.doi.org/10.1016/j.coastaleng.2019.103528.

Viviano, A., Naty, S., Foti, E., Bruce, T., Allsop, W., Vicinanza, D., 2016. Large-scale experiments on the behaviour of a generalised oscillating water column under random waves. Renew. Energy 99, 875–887. http://dx.doi.org/10.1016/j.renene.2016.07.067.

Welch, P., 1967. The use of fast fourier transform for the estimation of power spectra: A method based on time averaging over short, modified periodograms. IEEE Trans. Audio Electroacoust. 15, 70–73. http://dx.doi.org/10.1109/TAU.1967.1161901.

Weller, H.G., Tabor, G., Jasak, H., Fureby, C., 1998. A tensorial approach to computational continuum mechanics using object-oriented techniques. Comput. Phys. 12, 620–631. http://dx.doi.org/10.1063/1.168744, http://arxiv.org/abs/https://aip.scitation.org/doi/pdf/10.1063/1.168744, https://aip.scitation.org/doi/abs/10.1063/1.168744.

Windt, C., Davidson, J., Ringwood, J.V., 2018. High-fidelity numerical modelling of ocean wave energy systems: A review of computational fluid dynamics-based numerical wave tanks. Renew. Sustain. Energy Rev. 93, 610–630. http://dx.doi.org/10.1016/j.rser.2018.05.020, https://www.sciencedirect.com/science/article/pii/S1364032118303629.

Windt, C., Davidson, J., Ringwood, J.V., 2021. Investigation of turbulence modeling for point-absorber-type wave energy converters. Energies 14, http://dx.doi.org/10.3390/en14010026, https://www.mdpi.com/1996-1073/14/1/26.